Recording laser-induced sparks on Mars with the SuperCam microphone

Baptiste Chide, Sylvestre Maurice, Agnès Cousin, Bruno Bousquet, David Mimoun, Olivier Beyssac, Pierre-Yves Meslin, Roger C. Wiens

To cite this version:

Baptiste Chide, Sylvestre Maurice, Agnès Cousin, Bruno Bousquet, David Mimoun, et al.. Recording laser-induced sparks on Mars with the SuperCam microphone. Spectrochimica Acta Part B: Atomic Spectroscopy, 2020, 174, pp.106000 -. 10.1016/j.sab.2020.106000 . hal-03492996

Recording Laser-Induced Sparks on Mars with the SuperCam Microphone

Baptiste Chide[a,b], Sylvestre Maurice[b], Agnès Cousin[b], Bruno Bousquet[c], David Mimoun[a], Olivier Beyssac[d], Pierre-Yves Meslin[b], Roger C. Wiens[e]

[a] *Institut Supérieur de l'Aéronautique et de l'Espace (ISAE-SUPAERO), Université de Toulouse, 31400 Toulouse, France*
[b] *IRAP-CNRS, Université Toulouse III, 31400 Toulouse, France*
[c] *Université de Bordeaux, CELIA, CNRS UMR 5107, 33400 Talence, France*
[d] *Sorbonne Université, Muséum National d'Histoire Naturelle, CNRS UMR 7590, Paris, France*
[e] *Los Alamos National Laboratory, Los Alamos, NM 87545, USA*

Abstract

The SuperCam instrument suite onboard the Mars 2020 *Perseverance* rover includes a microphone used to complement Laser-Induced Breakdown Spectroscopy investigations of the surface of Mars. The potential of the SuperCam microphone has already been demonstrated for laser ablation under Earth atmosphere in a preliminary study (*Chide et al., 2019* [1]) with a small set of samples and fixed experimental conditions. This new experimental study, conducted under Mars atmosphere, explores all the main environmental, instrumental and target dependent parameters that likely govern the laser-induced acoustic signal that will be generated on Mars. As SuperCam will observe targets at various distances from the rover, under an atmospheric pressure that follows diurnal and seasonal cycles, this study proposes a sequence of corrections to apply to Mars data in order to compare acoustic signal from targets sampled under different configurations.

In addition, 17 samples, including pure metals but also rocks and minerals relevant to Mars' surface were tested to study the influence of target properties and laser-matter interactions on the acoustic signal and the ablated volume. A specific behavior is reported for metals and graphite, which rapidly disperse the incoming laser energy through heat diffusion. However, for other minerals and rocks, the growth of the crater is seen to be responsible for the shot-to-shot decrease in acoustic energy. As a consequence, it is confirmed that monitoring the acoustic energy during a burst of laser shots could be used to estimate the laser-induced cavity volume. Moreover, the amount of matter removed by the laser is all the more important when the target is soft. Hence, the decreasing rate of the acoustic energy is correlated with the target hardness. These complementary information will help to better document SuperCam targets.

Keywords: Mars, Mars 2020 *Perseverance* rover, SuperCam, Microphone, Acoustic, LIBS, Laser ablation, Rock hardness, Penetration depth

1. Introduction

Mars is not as quiet as one can imagine when considering the high sound absorption of the carbon dioxide that composes its low-pressure atmosphere [2]. Indeed, some acoustic waves, especially in the infrasound domain, do propagate and are characteristic of atmospheric phenomena such as dust-devil-like convective vortices [3] or baroclinic waves [4], as detected by the InSight mission. For outreach purposes, infrasounds detected by the InSight Auxiliary Payload Sensor Suite and vibrations captured by the short period seismometer were transposed in the audible. Unfortunately, no real sound recording in the audible range from 20 Hz to 20 kHz has been performed yet.

Scheduled for landing in Jezero crater in February 2021, the Mars2020 *Perseverance* rover will carry two microphones: one to capture acoustic signals during the entry, descent and landing of the vehicle [5] and the other one, part of the SuperCam instrument suite [6, 7], is designed to operate during surface mission, in combination with the SuperCam Laser-Induced Breakdown Spectroscopy (LIBS) technique. This study focuses on the latter which is located on top the rover mast and co-aligned with the LIBS telescope boresight. It will record laser-induced sparks in the 100 Hz to 10 kHz frequency range, during LIBS analysis, with a sampling rate of 25 kHz or 100 kHz. The microphone's primary objective is to support SuperCam's LIBS investigation, but it will also contribute to atmospheric science: it will monitor wind-induced signals to estimate wind speed and direction [8] and it will infer air temperature through the speed of sound when determining the arrival time of the LIBS sound wave [9]. In addition, it will provide diagnosis information on the operation of companion payloads such as MOXIE or the rover's drill.

The intensity of a laser-induced acoustic signal was experimentally shown to be an indicator of the ablation process (see [10] for a detailed review of the experimental applications of shock-waves in laser-induced plasma). More specifically, after firing 10,000 shots on aluminum-oxide ceramics, Grad and Možina [11] noticed a decreasing shot-to-shot evolution of the acoustic signal with different regimes as a function of the number of shots, attributed to different phases of the ablation crater development, whose transitions depend on the target composition. Moreover, the target that had the lowest ablated volume corresponded to the target that had the smallest difference of the acoustic signal amplitude between the first and the last shots. Similar regimes of the acoustic energy along a depth profile have been observed under Mars atmosphere [12], but the link with the ablated volume was missing.

Our previous experimental study, conducted at Earth pressure and atmospheric composition (Chide et al. [1]), related the laser-induced acoustic signal with laser-induced crater volume and LIBS optical spectrum intensity. For a small set of eight samples, the acoustic energy was shown to decrease with a rate that is dependent on the hardness of the target. For softer targets, the sharp decrease of the acoustic energy was linked with the rapid growth of the laser-induced crater whereas for harder targets, the almost constant acoustic energy corresponded to a low ablation rate. Additionally, a singular behavior of the acoustic energy was observed on the iron-nickel target which had a constant acoustic energy but a low hardness. Correlating the acoustic energy and the ablated volume together has highlighted a linear relationship between these two quantities: by monitoring the relative acoustic energy between the first and the last shots of a laser burst, it is possible to estimate the ablated volume after this given number of shots. These two results represent valuable information in the context of the *in situ* exploration of the surface of Mars with SuperCam for instance to characterize rock coatings [13]. Therefore, it is an expected and necessary step to extend this study to Mars atmosphere (low pressure, CO_2 composition) as the properties of the background medium influence both the laser-induced plasma parameters and the acoustic wave propagation. Moreover, this present work uses a larger set of samples including metallic targets important for understanding the physical mechanisms generating the acoustic signal and with mineral phases expected to be found on Mars in Jezero crater.

In contrast to laboratory experiments where each parameter can be changed independently of the others, once on Mars, many instrumental and environmental parameters will change from one target to another. Thus, in order to precisely understand the acoustic signal recorded for several targets of different natures, it is a prerequisite to characterize all the parameters that influence the acoustic signal and estimate their sensitivity. Section 2 details a literature review of these parameters that can be grouped into three categories: instrumental, environmental and target-dependent. After a description, in Section 3, of the setup used in this study, Sections 4 and 5 present the behaviors of the acoustic signal when changing experimental conditions and target nature. Finally, Section 6 summarizes the information on the SuperCam Microphone to support LIBS investigation on Mars, and how the acoustic energy can be used to estimate the target hardness and the ablated volume.

2. Generation of the Laser-Induced Spark

As a laser beam illuminates a sample, its initial energy is converted into heat and transferred within the material. Above a certain threshold energy, ablation of the material occurs: the surface suffers a sudden and sharp increase in temperature leading to a sample mass removal due to vaporization. This vapor is ionized and forms a plasma plume whose pressure is significantly higher than the background pressure leading to the formation of a strong shock wave. The whole process is very complex and involves strongly non-linear phenomena. As a matter of fact, laser ablation, vapor expansion and shock-wave propagation are sensitive to parameters from different origins, including: laser beam characteristics that control the energy reaching the sample, target properties that govern the efficiency of the laser-matter interaction, and environmental parameters that influence plasma dynamics and the propagation of the acoustic waves. We will discuss these in turn.

2.1. Instrumental parameters

The laser pulse properties and focusing conditions are key instrumental parameters that control the maximum energy per unit of surface available for target ablation and then strongly influence the LIBS optical and acoustic signal. The ablation process is more efficient when the laser output energy is high. However this process also depends on the surface area over which the energy is spread (giving the laser fluence in $\mathrm{J\,cm^{-2}}$) and the pulse duration which determines the irradiance (in $\mathrm{GW\,cm^{-2}}$). For laser pulses lasting a few nanoseconds or longer, the pulse width is also critical, as nanosecond laser pulses partly interact with the expanding plasma and one can observe plasma heating and plasma shielding of the surface [14].

From an acoustic point of view, the sensitivity of acoustic shock-wave parameters with various laser energy and focusing conditions for breakdown of atmospheric air was explored in Manikanta et al. [15, 16]. The peak-to-peak acoustic signal pressure increases linearly within the range of laser energies tested and decreases as the beam diameter at the focal plane increases. Acoustical monitoring of the ablation process [17, 18] showed that there is a linear link between acoustic signal and laser fluence. A similar linear relationship was established between the laser fluence and the ablation rate [19, 20]. The comparison between the four aforementioned studies suggests a potential correlation between the acoustic signal and the ablation rate but no causal link has been clearly established.

2.2. Target properties

The targeted material properties govern how efficiently the laser power is converted to ablation. These so-called matrix effects tend to complicate the quantitative compositional analysis with LIBS, as the change in laser-matter interactions between targets can affect the amount of ablated mass and the plasma properties [21].

Coupling of the energy from the incoming laser pulse depends on the target's optical properties at the laser's wavelength. The laser radiation is absorbed by the material via the Beer-Lambert law over the optical penetration depth δ_{opt} which is defined by the inverse of the absorption coefficient of the sample. The shorter the optical penetration depth is, the more energy per unit of volume is available for ablation. The reflectivity of the material also determines the fraction of the laser beam that is allocated for ablation, however the behavior of this coefficient is sharply changing during the laser pulse due to rapid changes in surface temperature and surface roughening [22, 23]. The laser energy absorbed within the sample is then converted into thermal energy and is propagated into the material via heat conduction depending on its thermal properties. The thermal penetration depth δ_{th} can be defined as a function of the thermal diffusivity and the laser pulse duration: $\delta_{\text{th}} = \sqrt{D\tau} = \sqrt{\frac{k}{\rho C_p}\tau}$ with D being the thermal diffusivity, τ the laser pulse duration, k the thermal conductivity, ρ the material density and C_p the heat capacity. For high-diffusivity materials, absorbed heat diffuses quickly, yielding less vaporization [21]. These concepts were used in Fau et al. [24] for the simple case of the ablation of hematite. It should be kept in mind that these aforementioned assumptions apply for purely uniform monocrystalline samples with homogeneous optical and thermal properties. In the case of microcrystalline assemblies likely to be encountered on Mars, laser-matter interaction, laser beam absorption and heat diffusion might be even more complex.

Firing successive laser shots at the same location on a target creates a crater that changes the laser-matter interaction. As the laser penetrates into the sample [25], the plasma is more confined inside a cavity, which leads to further changes in its physical parameters [19]. The laser-induced acoustic signal decreases with depth [11], and Chide et al. [1] found a linear relationship between the evolution of the ablated volume and the acoustic signal during a burst of laser shots on the same spot.

2.3. Atmospheric conditions

The shock-wave expansion has been theoretically described by the Taylor-Sedov blast-wave model [26, 27] assuming that a large amount of energy supporting the explosion is released in an infinitely small volume of perfect gas. This theory was verified experimentally [28], showing a hemispherical primary shock front propagating in the ambient gas at supersonic speeds up to $4 \times 10^3\,\mathrm{m\,s^{-1}}$ with a shock pressure up to 210 MPa. The shock wave becomes increasingly weaker with time and when the pressure behind the shock front approaches the order of magnitude of the atmospheric pressure, the blast-wave model is no longer valid and the pressure perturbation p propagates like a classical spherical acoustic wave [29]:

$$p(r) = \frac{p_0 r_0}{r} \exp(-\alpha r) \exp(i(\omega t - kr)) \tag{1}$$

with p_0 the pressure amplitude at a distance r_0, r the distance from the source, ω the angular frequency, k the wave number and α the total frequency-dependent atmospheric attenuation coefficient. It accounts for energy loss of the wave as it interacts with the ambient medium. Mechanisms involved in the attenuation are absorption due to viscosity, and thermal conduction, but also rotational and vibrational relaxation of the CO_2 molecules that compose more than 95% of the Martian atmosphere. They also depend on atmospheric pressure and temperature. Semi-empirical models developed by Bass and Chambers [30] and Williams [2] can be used to estimate the pressure damping due to the propagation into the atmosphere but have not been validated with experimental data from Mars. Unfortunately the link between the pressure of the shock front close to the source and the associated acoustic pressure recorded at longer distances is missing. The presence of wind may also affect the recording of laser-induced acoustic waves by producing microphone noise, downgrading the signal-to-noise ratio of the LIBS acoustic detection. However, wind-induced noise has a lower-frequency content that can be filtered out from the raw acoustic signal to retrieve the contribution of laser sparks [12].

The ambient pressure also plays a significant role in plasma plume confinement [31]. When the pressure is reduced down to 10 Torr, the plume extends to a larger volume, leading to a lower density plasma, optically thin, limiting the plasma shielding. At this pressure, a greater portion of the laser beam reaches the sample surface, allowing more energy for mass ablation.

To conclude this bibliographic study, all the parameters that were shown to play a role in the acoustic signal are listed in Table 1. It shows how there are coupled together in the different phases that of the acoustic signal generation and propagation.

		Laser Irradiance	Laser-target coupling	Sound Propagation
Instrumental Parameters	Laser Energy	√	-	-
	Focus Quality	√[1]	-	-
	Distance	√[1]	-	√[1]
Material Properties	Optical prop.	√[2]	√[2]	-
	Thermal prop.	-	√[2]	-
	Ablation cavity	-	√[1]	-
Atmosphere	Composition	-	√[2]	√[2]
	Pressure	-	√[1]	√[1]
	Temperature	-	-	√

Table 1: Summary of all the parameters listed in section 2 that are known to play a major role in the laser-induced acoustic signal. They are divided into three categories : instrumental, target-dependent and atmospheric. Each parameter is associated with a phase in the ablation process, from laser energy deposition at the surface of the target to energy diffusion inside the sample and sound generation and propagation. [1] highlights the parameters whose influence on the acoustic signal is described experimentally by an empirical relationship in the next sections. [2] highlights the parameters whose influence on the acoustic signal is assessed qualitatively in the next sections. The other ones were not tested experimentally.

3. Experiment description

3.1. A Martian LIBS setup combined with acoustics measurements

The Mars-atmosphere LIBS calibration test bench at Institut de Recherche en Astrophysique et Planétologie (IRAP, Toulouse, France) used the LIBS capability of the ChemCam Mast Unit Engineering and Qualification Model (infrared laser pulse at 1067 nm of about 10 mJ). The Mast Unit was coupled with the ChemCam Body Unit Engineering Model that includes three spectrometers collecting the light emitted from the plasma over the UV (240.1 nm to 342.2 nm), the violet (382.1 nm to 469.3 nm) and the visible plus near infrared (VNIR, 474 nm to 906 nm). More details on this setup can be found in other studies [24, 32, 33]. The full schematics of the experimental bench is represented in Fig. 1. The laser beam exiting the instrument was redirected into a vacuum chamber by a folding mirror which was also used to precisely adjust the pointing of the laser beam onto the sample.

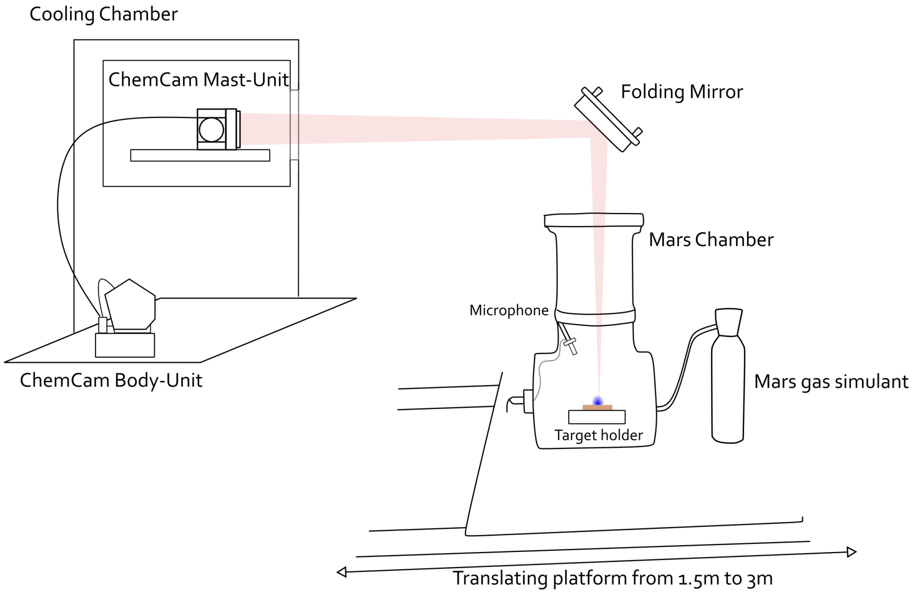

Figure 1: Schematic of the LIBS combined with acoustic test bench under Mars atmosphere.

The chamber was filled with a controlled Mars atmosphere (95.7% of CO_2, 2.7% of N_2 and 1.6% of Ar), the pressure of which can be adjusted between 1×10^{-1} and 10 mbar. Targets were placed on a horizontal aluminum support at the bottom of the chamber and the laser beam hits the targets perpendicularly to their surface. The chamber was mounted on rails to move it away from the instrument allowing an extension of the optical path length from 1500 mm to 3000 mm. This facility was also upgraded with a microphone, located about 25 cm away from the target, on the upper part of the chamber. It was pointed toward the targets. This microphone (same model as the SuperCam microphone) and its acquisition system were exactly the same ones that were used in [1]. The microphone recorded the LIBS burst continuously from the first shot to the last one at a sampling rate of 200 kHz.

3.2. Set of samples

Two different types of samples were used for these experiments. Five pure metals with tabulated and well known physical properties, and a set of natural homogeneous minerals graciously obtained from the Collection de Minéraux at Sorbonne Université, Paris, France.

They are listed in Table 2, along with basic physical properties that are expected to play a significant role in laser-matter interaction and acoustic signal. References for these properties are listed in the caption of the table. The gypsum, JSC-1 pellet, the black marble and magnetite are exactly the same samples as the ones studied under ambient conditions (hereafter defined as Earth atmosphere conditions) [1], and were used as a comparison between the two experiments. The Vickers Hardness was measured with a Micro Vickers Hardness Tester (Buelher MVK H1). The uncertainty in hardness presented in Table 2 is the standard deviation between the 3 to 5 measurements performed on each sample. All the samples were cut or carefully chosen to provide a planar surface to the laser beam and to avoid any surface roughness effects. A picture of all the targets is shown in Fig. 2. Most of the rocks and minerals selected for this study (with the exception of graphite and marbles), correspond to materials that have been identified on Mars [34, 35].

All the samples were selected for their homogeneity and their variety of thermal and optical properties to be compared with the acoustic signals. In particular, two categories can be formed regarding the thermal and optical penetration depths: metals and graphite that have a long thermal penetration depth compared to the optical penetration depth. These targets easily dissipate laser energy out of the optical absorption zone through thermal diffusion. Other targets have a short heat penetration depth so that the energy deposited by the laser remains localized in the absorption zone [36].

3.3. Experimental procedures

Several experimental protocols have been implemented to test the influence of experimental conditions or target properties on the acoustic signal each at a time:

i The influence of the background CO_2 pressure was tested by increasing the pressure inside the chamber from 1 mbar to 10 mbar by steps of 1 mbar. For each pressure level, a burst of 10 successive laser shots was performed on the titanium target. The location of the impact position was changed between each successive burst to prevent from any cavity

Type	Target	Density ($\mathrm{g\,cm^{-3}}$)	δ_{th} (nm)	δ_{opt} (nm)	Vickers Hardness	References
Metals	Aluminum	2.70	700	8	340 ± 8	[37]
	Copper	8.96	767	11	88 ± 1	[37]
	Iron	7.87	336	21	104 ± 6	[37]
	Lead	11.35	347	15	8 ± 1	[37]
	Titanium	4.51	216	26	286 ± 38	[37]
Fe-oxides	Hematite	5.15	140	7700	1367 ± 154	[38, 39, 40]
	Ilmenite	4.75	52	8.4×10^4	645 ± 76	[38, 39, 41]
	Magnetite$*$	5.17	92	229	767 ± 134	[38, 39, 40]
Carbon	Graphite	2.16	2497	41	23 ± 3	[37, 42]
Feldspar	Albite	2.62	70	8.5×10^6	250 ± 26	[43, 44]
Pyroxene	Enstatite	3.20	91	1.6×10^5	49 ± 8	[38, 45]
Sulfate	Gypsum$*$	1.00	28	-	3 ± 0.5	
Carbonates	Marble	2.71	82	-	124 ± 10	[39, 46]
	Black Marble$*$	2.69	82	-	177 ± 24	[39, 46]
Rocks	Argilite	2.60	70	-	9 ± 1	[47]
	JSC-1$*$	1.70	-	-	29 ± 7	
	Basalt	3.00	50	6.6×10^4	705 ± 97	[47, 48]

Table 2: Samples used in these combined LIBS and acoustic experiments and some of there physical properties when there have been found. Targets indicated with a star ($*$) are the same ones that were used in our previous Earth atmosphere study. The JSC-1 target is a pressed pellet of Martian regolith simulant [49] compacted with a load of 3 tons. The gypsum sample is a slice of plaster.

effects either on acoustic or spectral intensity. Distance from the instrument to the laser was set to 1650 mm. The acoustic energy and LIBS optical spectrum were monitored for each single shot.

ii The influence of the quality of the focus on acoustic data and LIBS spectra can be estimated using a focus stacking (z-stack technique), described in Le Mouélic et al. [50] for the ChemCam Remote Micro Imager. For the titanium, magnetite and enstatite targets, 18 bursts of 10 shots were fired at various distances around the best focus position. The best focus position was determined by the nominal autofocus capability of ChemCam that uses a continuous-wave laser diode. The best focus position is found when the flux back scattered from the target is maximum. This configuration of the telescope maximizes the laser irradiance deposited on the target and therefore it provides the maximum intensity of the emission spectrum [51]. Ten motor steps (corresponding to ~3 mm at this working

Figure 2: Pictures of all the samples detailed in Table 2. The laser craters created for this study are seen in almost all the targets. For some targets, multiple craters resulting from other experiments can also be seen.

distance of 1650 mm) separated each consecutive focus distance. The CO_2 pressure was set to 6.2 mbar for this experiment. Acoustic data and LIBS spectra were recorded for each laser shot in the same way as previously described. The impact position of the laser was shifted slightly between each successive burst so that the LIBS craters did not superimpose each other.

iii To test the influence of the laser-to-target distance, the titanium target was set at four increasing distances from the instrument (1656, 1885, 2402 and 2828 mm). For each position of the target, an autofocus was performed to measure precisely the optical path length, followed by 3 bursts of 30 shots. The pressure was set to 6.1 mbar.

iv The behavior of the acoustic signal with respect to the nature of the target was tested by using the full set of samples described in Table 2. Targets were positioned at $\sim$1650 mm with only slight variations between each distance depending on their thickness ($\pm$ 10 mm). For each target bursts of 10, 30, 90 and 150 shots were repeated 2 times (or 3 depending on the space available on each target) at different locations. The background pressure was set to 6.2 mbar with variations of $\pm$ 0.3 mbar during the time of the experiments. An autofocus was performed at the center of each target; the precision on the optical path length is $\pm$ 0.5% of the total distance [52]. For this experiment, the volume of each cavity was analyzed with a non-contact 3D surface profiler (Sensofar S-NEOX) using either confocal or interferometry scanning. The volume is computed as the integral under the mean plane of the pristine surface. For the lenses used, the uncertainty on the depth of each pixel was ± 0.5 µm. Therefore, the measurement uncertainty on the volume is computed as the surface of the crater multiplied by the uncertainty on the depth. For small craters of 1×10^5 µm^3 (see craters in metals in section 5.1) the relative uncertainty is about ± 50% of the total volume. For craters bigger than 1×10^6 µm^3 the uncertainty on the volume is lower than ± 5%. In the following sections, for each figure presenting the ablated volume, a secondary axis displays the associated mean depth which was computed as the average depth between several profiles of each crater.

3.4. Measurements

Unlike our previous study at ambient pressure in which we used an anechoïc chamber, such a chamber was not used in this work, as it was not possible to adapt an anechoïc chamber for low pressures. The aluminum chamber where the microphone was operated during this study contributed to significant sound reflections. Hence, a careful check of the waveform recorded in the chamber had to be made to be sure that a direct signal was obtained without an echo. Fig. 3a displays a typical LIBS acoustic waveform recorded by the microphone inside the chamber filled with ∼6 mbar of Mars gas simulant. It shows that the first compression is recorded with no echo superposition and that the first echo arrives 46 µs after the arrival of the direct acoustic signal. Considering a sound speed of 273 m s^{-1} at 23 °C it corresponds to a propagation distance of 1.2 cm. It matches with a sound reflection on the aluminum plate that holds the samples, the black marble target used for this example being ∼0.6 cm thick. After that, many echoes are observed in the time series due to multiple reflections on the chamber walls. All the echoes were dissipated before the next laser pulse, which repeated every 333 ms. Two characteristic measurements could be performed on this acoustic wave: the maximum amplitude of the compression (the shock-wave amplitude in Pa) defined as the highest pressure point in the waveform, and also the acoustic energy (in Pa^2.s) which is the square value of the waveform, time integrated over the compression phase. This parameter was already used in other LIBS acoustic studies [53, 54, 55] over the entire waveform, but here it is restricted only to the compression phase not to integrate echoes. Experimental data show that the acoustic energy is proportional to the square of the shock-wave amplitude. Later in this study, the acoustic energy will be presented as a representative parameter of the acoustic signal, as it is computed over more data points than the shock-wave amplitude. Nonetheless, each figure will also present the corresponding shock-wave amplitude in a secondary y-axis.

A typical LIBS optical spectrum acquired by the ChemCam spectrometers is displayed in Fig. 3b for the same shot and the same target as its associated acoustic signal represented in Fig. 3a. Each spectrum is processed following the data pipeline described in Wiens et al. [56], including de-noising and wavelength calibration. However the continuum produced by Bremsstrahlung and recombination radiations was not removed from these spectra. The area under the curve in the VNIR range, including the continuum (spectral region within the shaded rectangle in Fig. 3b) will be used as a parameter representative of the LIBS optical emission intensity because this spectrometer covers the largest spectral range and it has by far the strongest contribution to the continuum [56]. Because the goal of this paper is to study the acoustic signal, this simple spectral parameter will only be used in comparison with the acoustic energy.

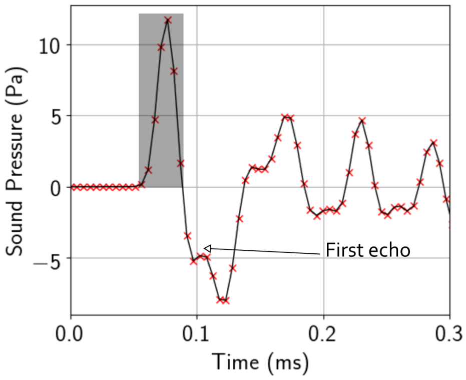

(a)

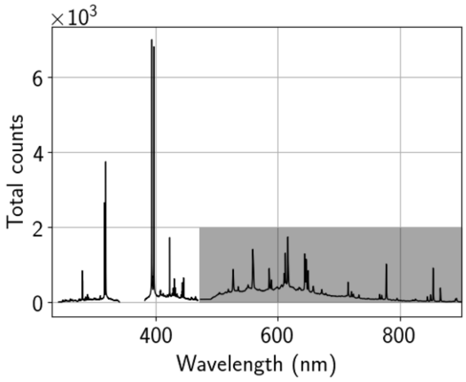

(b)

Figure 3: (a) Typical LIBS acoustic waveform recorded by the microphone at 25 cm for the black marble target inside the vacuum chamber filled with ∼6 mbar of Mars gas simulant. The shaded area that covers the first compression is the domain used for the computation of the acoustic energy. (b) Typical LIBS optical spectrum acquired for the same laser shot on the black marble. The area below the spectrum in the VNIR range (shaded rectangle) is used as an indicator of the LIBS spectrum intensity.

4. Influence of Experimental Parameters

Experimental conditions when using LIBS on Mars are always changing depending on the properties of the selected target, and also on the local climate that controls the daily and seasonal cycles of the atmospheric pressure. On the one hand, the irradiance deposited on the target is the key instrumental parameter that governs the efficiency of the ablation. For both SuperCam and ChemCam, the irradiance depends on the offset between the distance retrieved by the autofocus algorithm and the real optical path length between the laser and the sample surface (the quality of the focus for a given distance). But it also depends on the distance from the laser to the target, as the optimal beam radius increases with the distance of the target [52]. On the other hand, the background pressure plays a role in the laser-induced plasma expansion. As these experimental parameters influence the ablation process, they also have an impact on the shock-wave generation and propagation. Therefore, this section studies the sensitivity of the laser-induced acoustic signal with respect to these parameters. Finally, a comparison between the results obtained under Earth atmosphere and Mars atmosphere is presented: these result from changes in both the pressure and the atmospheric composition.

4.1. The impact of atmospheric pressure variation

The variation of the laser-induced shock-wave energy as a function of the background CO_2 pressure is represented in Fig. 4 and compared with the evolution of the LIBS optical spectrum intensity. It shows that the acoustic signal is an increasing function of the background pressure, likely due to an increase of the atmospheric density leading to stronger shock-waves. It is obviously silent when the laser is fired under vacuum whereas a plasma is created and its light collected by the telescope. Then the acoustic energy increases linearly between 2 mbar and 8 mbar, a range that covers the typical daily and seasonal variations of the Mars atmospheric pressure [57]. It has to be noticed that the acoustic energy increases by $\sim 50\%$ between 6 and 8 mbar. The LIBS spectrum intensity also increases linearly but less sharply than the acoustic energy. Above 9 mbar the acoustic energy has lower values than the fitted

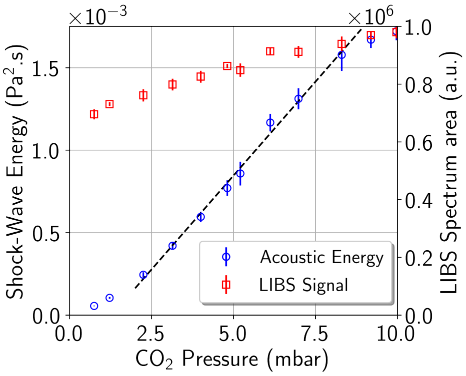

Figure 4: Median acoustic energies over 10 shots at various CO$_2$ pressure for the titanium target (blue circles). Black dashed line represents a fit of the linear portion of the curve between 2 mbar and 8 mbar ($y = 2.272 \times 10^{-4}x - 2.974 \times 10^{-4}$). It is compared with the median over 10 shots of the LIBS spectrum area (in the VNIR) for each series of shots (red squares). Both for the acoustic energy and the LIBS spectrum area, error bars represent the standard deviation over the 10 shots performed at each pressure.

linear model. This pressure may correspond to an increase in collision excitation in the plasma and the effect of its confinement.

4.2. *Effects of the quality of the focalisation*

The LIBS sound level is often used by LIBS teams in their laboratory to rapidly find the optimal focus of their LIBS setup. In this section the influence of the focus quality on the laser-induced acoustic signal is investigated. As observed under ambient pressure [58], different acoustic behaviors were observed between irons oxides and other minerals. Therefore, this experiment was conducted over three targets of different natures: one metal, one iron oxide and one high absorption mineral (an enstatite).

Fig. 5 shows the evolution of the acoustic energy for different distances around the best focus position for the enstatite, magnetite and titanium. Values are normalized by the acoustic energy measured at best focus. First, for the three targets, the median acoustic energy over the 10 shots is at its maximum around the best focus distance and decreases as we move away from this position. It is observed that out-of-focus laser footprints cover a larger surface. The laser energy deposited per unit of surface is smaller, leading to a less efficient ablation.

It can be noticed that these curves are not symmetric on both sides of the maximum, *i.e.* the mean acoustic energy decreases faster when the focal point is outside the sample than when it is inside. For the titanium target, when the focal point is 10 mm inside the sample, the acoustic energy falls by 17% compared to the one recorded around the best focus, whereas it falls by 50% when the laser is focused 10 mm above the surface of the sample. At best focus a difference in sound level is seen between the three targets: $1.54 \times 10^{-3}\,\mathrm{Pa}^2\,\mathrm{s}$ for titanium, $1.25 \times 10^{-3}\,\mathrm{Pa}^2\,\mathrm{s}$ for magnetite and $0.44 \times 10^{-3}\,\mathrm{Pa}^2\,\mathrm{s}$ for enstatite. It will be discussed in section 6.3.

The Z-stack analysis is performed in order to measure the LIBS sound's depth of field with respect to the distance from the best focus position. Therefore, the acoustic depth of field is defined as the distance range over which the acoustic energy intensity is above 50% of its maximal value. Under these conditions, the values are 45.5 mm for magnetite, 33.5 mm for titanium and 14.3 mm for enstatite. At our working distance, it corresponds to an acoustic depth of field of 2.7%, 2.0% and 0.9% of the target distance. This large difference between the enstatite and the two other targets could be explained by a lower laser coupling for enstatite (it has by far the largest optical penetration depth). Therefore, for the enstatite, the irradiance may fall below the ablation threshold faster than for the two other targets.

Because the acoustic depth of field is a new parameter, it can be compared with the depth of field computed from the LIBS signal that is more often used. Fig. 5 compares the median LIBS spectrum intensity in the VNIR range over the 10 shots with the median acoustic energy as a function of the distance from best focus for titanium, magnetite and enstatite. The LIBS signal follows the same variations as the acoustic energy. For the magnetite, the acoustic energy curve is slightly larger than the LIBS signal intensity curve whereas for titanium the acoustic energy curve is narrower than the LIBS signal intensity curve. However, acoustic and optical spectrum depths of field are very close to each other.

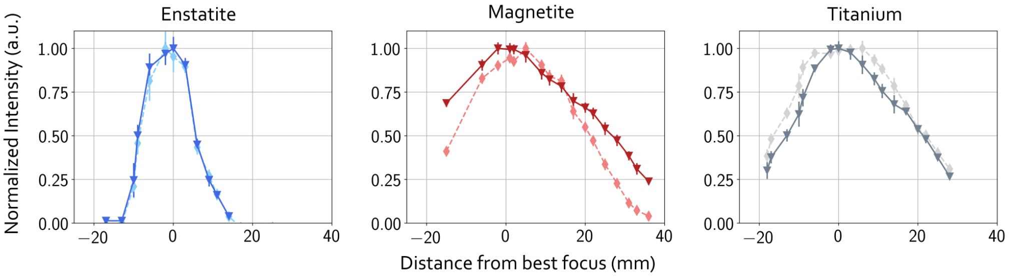

Figure 5: Normalized sound energy (solid darker line) compared with normalized LIBS spectrum intensity (lighter dashed line) at various distances from the best focus position for the three target where z-stacks were performed. Absolute values of the acoustic energy are detailed in the text. The error bars represent the standard deviation of the measurements over the burst of 10 shots. Negative distances correspond to a focal point above the target surface whereas positive distances correspond to a focal located inside the target.

Consequently, acoustic Z-stacks can be used as a focus method for the telescope and it is shown to be as accurate as the LIBS spectra Z-stack method that was used with ChemCam on Mars after the autofocus anomaly occurred (season 2 data, [59]). Acoustic depth-of-field differences between metallic targets and enstatite, will be considered in Section 6.3 to estimate the uncertainty on the amplitude of the acoustic energy relative to the uncertainty on the focus.

4.3. Effects of the variation of the laser-to-target distance

Both the focus quality and the laser-to-target distance constrain the irradiance deposited on the target but the increase of the laser-to-target distance induces an additional effect on the acoustic signal due to the propagation of sound through a longer path. The impact of the loss of irradiance with the increase of laser-to-target distance on the acoustic energy and the LIBS optical spectrum is represented in Fig. 6 for the titanium target. For each distance, two experimental points are the median over two bursts of 30 shots and two quantities are represented: the acoustic energy (blue) and the total intensity of LIBS spectra in the VNIR range (red). It is compared with an estimation of the evolution of the irradiance deposited on target as a function of the distance for the LIBS setup used in this study, the data for which are extracted from Rapin [60]. Fig. 6 shows that the acoustic energy decreases the same way as the irradiance whereas the LIBS optical spectrum intensity falls faster. Indeed, the field of view of the collection area of the telescope increases with the distance [52], whereas the plasma size remains the same. Consequently, photon flux collected by the instrument decreases with the distance. This effect is combined with the decrease of the irradiance with the distance.

It should be noticed that for these experimental conditions, the distance from the microphone to the target is fixed (25 cm), therefore all the points are attenuated the same way by the atmospheric propagation. For this short propagation distance, it can be considered that the atmospheric attenuation is negligible, therefore the acoustic energy is considered not attenuated. However, on Mars, the increase of the instrument-to-target distance will also increase the propagation distance of the acoustic wave, therefore reducing the measured acoustic energy following Equation 1. The blue dashed curve in Fig. 6 represents the acoustic energy, taking into account the propagation distance (the attenuation coefficient considered is $0.05\,\mathrm{m}^{-1}$, extracted from Bass and Chambers [30] at 220 K and 2 kHz). The propagated acoustic energy represented in Fig. 6 is amplified by a factor of 65 for display purposes, to show it on the same plot as the other properties. To give an order of magnitude of the impact of the propagation on the amplitude of the acoustic energy, at 1500 mm the acoustic energy goes from $1.4 \times 10^{-3}\,\mathrm{Pa}^2\,\mathrm{s}$ without negligible propagation to $2.24 \times 10^{-5}\,\mathrm{Pa}^2\,\mathrm{s}$ when the propagation is taken into account. Therefore, one can note that on Mars, due to sound atmospheric attenuation, the acoustic energy is expected to decrease much faster than the intensity of the LIBS spectrum with the distance from the instrument.

4.4. Comparison between Earth and Mars atmosphere

The difference between ambient atmosphere and Mars atmosphere conditions is provided by the comparison of laser-induced sound evolution for the gypsum, JSC-1, black marble, and magnetite targets that were tested with both setups (see section 3.2). All the instrumental parameters were the same between the two studies with the exception of the optical path length that was ∼100 mm longer for the Earth study. Data under Earth atmosphere are

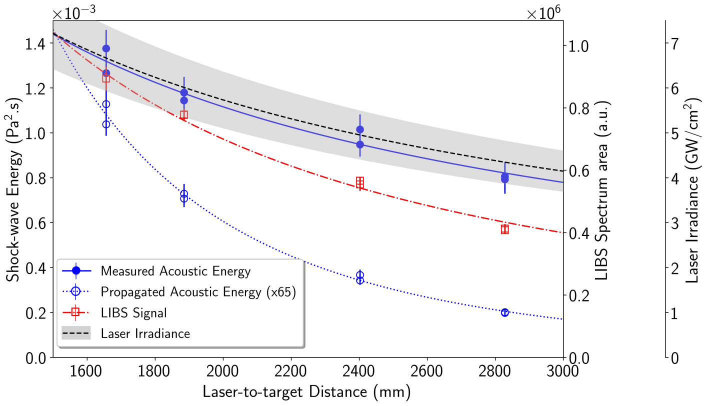

Figure 6: Evolution of the acoustic energy from a plasma on the titanium target as a function of the laser-to-target distance. The microphone was located at a fixed distance of ~25 cm from the target inside the Martian chamber. Each experimental point is the median acoustic energy over 30 successive shots at the same location. Both for the energy acoustic and the LIBS signal, error bars represent the standard deviation over the 30 shots performed. Two series of 30 shots were performed for each distance. Experimental points are represented with a power law ax^b that best fits the data (blue solid line, $y = 0.933x^{-0.8853}$). The blue dashed curve is the same acoustic energy but reduced to simulate the propagation into a Mars atmosphere along the distance in the x-axis. In this plot it is amplified by a factor of 65 to compare its evolution with other represented values. The sound attenuation coefficient considered values $0.05\,\mathrm{m}^{-1}$, which is extracted from [30] at 220 K and 2 kHz (see Equation 1 for the propagation law). LIBS spectrum median intensity (in the VNIR range) for each series of shots is represented by red squares also fitted with a power law (dashed red line, $y = ax^{-1.38}$). These experimental results are compared with an estimation of the irradiance on target for this LIBS setup, the data for which are extracted from [60]. The uncertainty on this law (shaded area) is ± 11% and is dominated by the uncertainty of the energy of the pulse for this setup.

extracted from Chide et al. [1].

Figure 7a presents the evolution of the normalized acoustic energy over 150 shots for the four targets under Mars atmosphere and compared with results obtained under Earth atmosphere. Although absolute energies are not presented in this figure, the acoustic energy is about 3 to 9 times greater (depending on the target) under 1 bar of air than under 6 mbar of CO_2 because of the difference in air density between the two experiments. But more surprisingly, for a given target, the evolution of the acoustic energy normalized by the first shot value, follows the same decrease for the two experiments. Looking at the evolution of the ablated volume could help to understand this similar trend seen between the two atmospheric conditions. Figure 7b shows the laser crater volume as a function of the number of shots for the terrestrial and Mars studies. Both experiments show a higher ablation rate during the first

~ 30 shots, then an almost linear increase of the ablated volume for a higher number of shots. More importantly, for each target, the ablated volume is of the same order of magnitude for ablation under a 6 mbar of Mars atmosphere and under 1 bar of air. After 150 shots, the ablated volume in the JSC-1 pellet is 28% larger under Earth atmosphere whereas it is 24% smaller under Earth atmosphere for the black marble compared to the ablation under Mars atmosphere. One could argue that for a higher surrounding pressure, the plasma shielding is more important, leading to a small fraction of the laser beam reaching the surface. However, Iida [61] showed that not only does the static pressure play a role in the ablation process, but properties of the surrounding gas such as the thermal conductivity and ionization energy also play a role. For instance the ablation rate under 1 mbar of air is almost the same as under 1 bar of helium, with a ratio that also depends on the nature of the target [14]. Therefore the different compositions of air and CO_2, may be responsible for the similar ablation rates observed between the two experiments, counteracting the effects of pressure. In addition, the comparable ablated volumes between Mars and Earth atmosphere explains the same decrease of the acoustic energy as a function of the number of shots. Indeed, it was previously shown [1] that the decrease of the acoustic energy is linearly linked with the ablated volume.

For the gypsum target, the deviation between volume measurements for the same number of shots increases significantly after the 90^{th} shot, compared to the other targets. Fig. 8 compares typical profiles of laser craters formed on the gypsum and on the JSC-1 pellet, under Mars atmosphere. It shows that after 90 shots, the gypsum crater has a more irregular shape and a larger diameter than the crater resulting from 30 shots. Moreover, the profile has a triangular shape compared to the smooth Gaussian profile for craters created in the JSC-1. It may be due to the brittleness of the gypsum target, the material of which is not only vaporized but also easily ejected with the pressure wave, resulting in a less repeatable volume between two craters with the same number of shots.

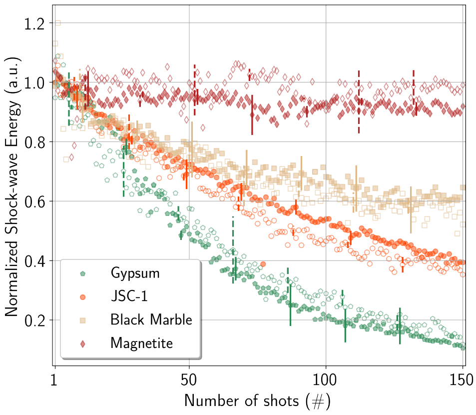

(a)

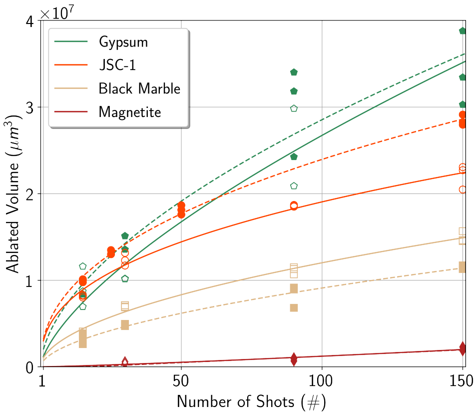

(b)

Figure 7: (a) Evolution of the acoustic energy for 150 successive shots at the same location for four targets ablated under Mars atmosphere (filled markers) and Earth atmosphere (unfilled markers). For each target, values are the mean between two (or three) bursts of 150 shots and data are normalized by the energy of the first shot. Error bars, displayed every 20 shots, represent the standard deviation between the three (or two for the magnetite) acquisitions per sample. (b) Evolution of the ablated volume as a function of the number of shots for the four targets compared between Mars (filled markers) and Earth atmosphere (unfilled markers). They are best fitted with a power law ax^b (solid line for Mars atmosphere and dashed line for Earth atmosphere). Note that for the JSC-1 pellet under Earth atmosphere, there was no experiment that created a crater for 90 shots but craters were made of 50 shots instead. For 150 shots under Mars atmosphere, volume measurements for the gypsum are missing. For the magnetite both curves are almost superimpose at this scale.

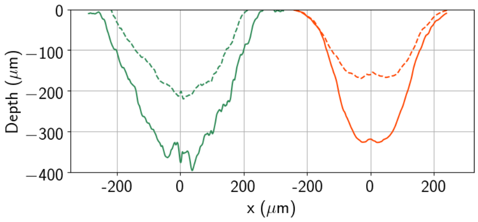

Figure 8: Typical profiles for laser craters made on the gypsum target (left, green) and on the JSC-1 pellet (right, orange) resulting from 30 shots (dashed lines) and 90 shots (solid lines) under Mars atmosphere.

5. Influence of target properties

This section compares the recorded acoustic energy and the measured ablated volume for all the targets presented in Table 2, which were sampled under a simulated Mars atmosphere.

5.1. The case of metals

Here we will discuss metallic targets separately from rocks and minerals, as they are observed to behave differently and are less relevant to targets expected on Mars, with the exception of iron meteorites [62] and titanium LIBS calibration targets [63]. Indeed, for nanosecond laser pulses, the thermal penetration depth is larger than the optical penetration depth (see Table 2) leading to a greater energy loss into the sample by thermal diffusion [64], and resulting in melting of some material around the laser-induced crater.

Fig. 9 shows the evolution of the acoustic energy and the ablated volume for the five metals tested in this study. For all the targets, the acoustic energy (Fig. 9a) shows a sharp decrease during the 3 first shots, and then remains almost constant during the rest of the burst. Only the lead signal decreases with a linear trend after the initial collapse and the copper signal slightly increases after 70 shots (see arrow highlighting this trend in Fig. 9a).

Craters formed in the lead sample are deep, with a conical shape and they display a rim which is higher than the pristine surface. Craters on other metals are shallow, and at their bottom, they present an irregular floor made of molten-like metal. Some molten ejecta material is seen near the location of the impact as if it was ejected during the pulse. Moreover, the ablated volume of copper, iron, titanium and aluminum is very small: the maximum is

$2 \times 10^6\,\mu m^3$ for 150 shots on aluminum compared to more than $1 \times 10^7\,\mu m^3$ for the same number of shots for lead. This large amount of vaporized lead compared to other metals was also observed in Iida [61] and attributed to lower change-of-state temperatures for lead compared to other metals.

Considering these observations, the shallow ablated craters explains that the acoustic energy is almost constant for iron, copper, aluminum and titanium, contrary to lead where its linear decrease could be explained by the higher ablation of the sample that created a deep crater. The large drop in acoustic energy during the 3 first shots, characteristic of metals, was already observed on aluminum by Lu et al. [65], and was considered as surface cleaning, such as the removal of a thin oxide layer. The same study also noticed the constant regime of the acoustic energy for higher numbers of pulses. In a follow-up study focused on copper samples, Lu et al. [53] noticed the increase of acoustic energy specific to copper and attributed it to surface morphology changes inside the laser spot, leading to modification of copper optical properties. Indeed, pristine copper has a very high reflectivity coefficient compared to other metals tested here (R$= 0.94$ at 1067 nm) and it must drop to significantly lower values with the roughening of the surface due ablation. Therefore, for copper, the reduction of the reflectivity coefficient increases the fraction of laser energy available for ablation. The difference in absolute values of the acoustic energy between different metals shown in Fig. 9a was also pointed out in Lu et al. [65] but was left unresolved. It will be discussed in Section 6.3.

5.2. The case of minerals and rocks

Depth profiles of 150 shots were conducted on all the other targets; the acoustic energy as a function of the number of shots is represented in Fig. 10 only for five of the targets. The absolute acoustic energy of the beginning of the sequence differs depending of the nature of the target. Most of the targets are grouped between $1 \times 10^{-3}\,Pa^2\,s$ and $2 \times 10^{-3}\,Pa^2\,s$ (corresponding to amplitudes from 9 Pa to 13 Pa) whereas the marble and the argilite lie around $3.2 \times 10^{-3}\,Pa^2\,s$ (equivalent to 17 Pa) and graphite at $7 \times 10^{-3}\,Pa^2\,s$ (27 Pa). This variation of the absolute acoustic energy, possibly a function of the nature of the material, is

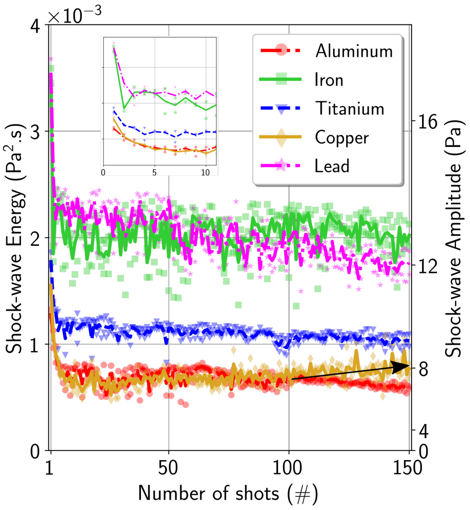

(a)

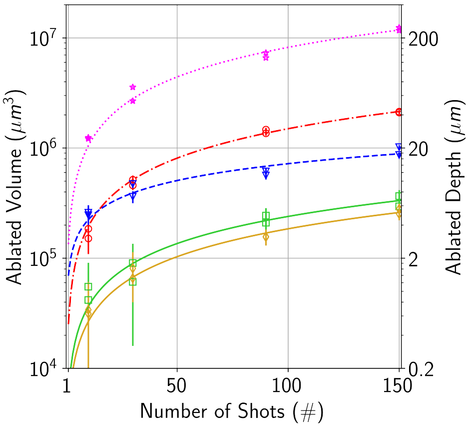

(b)

Figure 9: Evolution of the acoustic energy and shock-wave amplitude (a) and the ablated volume and depth (b) over 150 shots for the five metallic targets. For the acoustic energy, the two series of 150 shots at 2 different locations are represented by the symbols and the mean over these two series is represented by the colored line. The inset in (a) shows a close-up view over the first ten shots. The black arrow highlights the increasing trend for copper. For each target, two craters with the same number of shots are performed. The volume is fitted with a power function ax^b. Details on the error bars for the volume measurements are provided in Section 3.3. The logarithmic scale representation makes the error bars of the biggest craters barely visible.

discussed in Section 6.3, considering the sensitivity of the acoustic signal with regard to the quality of the focus, the background pressure and the distance.

Our previous study performed under Earth atmosphere has shown that the evolution of the acoustic energy could be represented by a decreasing exponential function; its exponential decay rate is correlated with the hardness. Here under Mars atmosphere, as with the Earth atmosphere experiments, the decay rate of the acoustic energy is a decreasing function of the hardness. The acoustic energy of graphite (soft mineral) has dropped by 30% in 150 shots whereas it has been reduced by only 6% for hematite (hard mineral). Although a decreasing exponential function was used to represent the evolution of the acoustic energy over 300 shots under Earth atmosphere, it does not perfectly fit this new data set, especially during the first shots. Indeed, targets can be grouped into two categories regarding the shot-to-shot evolution of the acoustic energy: the first group, which corresponds to the softer targets, shows a slope change of the acoustic energy after the first tens of shots. This can be seen for instance for the graphite, marble and gypsum in Fig. 10, with slope changes observed around the 20th, 50th and 70th shots, respectively. Targets belonging to this first group are gypsum, JSC-1, graphite, argilite, marble, black marble and basalt. This characteristic evolution of the acoustic energy can be fitted with two linear functions, one before and one after the slope change. For this set of targets, the acoustic energy decreases faster during the first regime than after the slope change. The second group is composed of harder targets where no slope change is seen (hematite, magnetite, ilmenite, enstatite and albite); see for example the magnetite in Fig. 10. It can be fitted with a linear function over the entire 150 shots of the burst.

The presence of a rapidly decreasing regime followed by a lesser slope regime had already been noticed by Murdoch et al. [12] for soft targets and in Chide et al. [1], not only with the acoustic energy, but also with LIBS spectral data. It was attributed to the growth of the laser crater leading to a loss of laser-material coupling due to both plasma shielding and steeper crater walls. Therefore, the evolution of the acoustic energy has to be studied in comparison

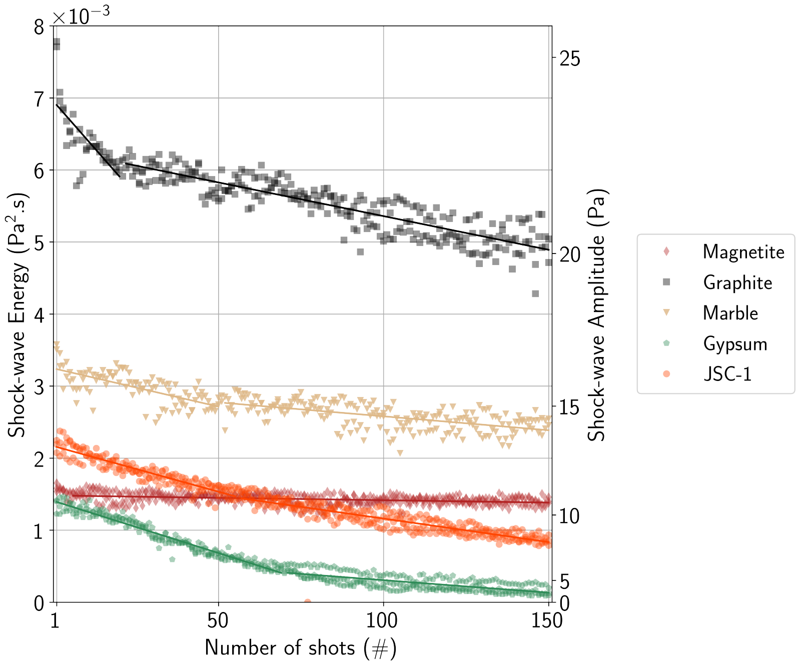

Figure 10: Variation of the acoustic energy (and shock-wave amplitude) during a burst of 150 consecutive shots on several targets. For each target the 2 (or 3) series of 150 shots at different locations are represented. Depending on the target, the mean of these series is fitted with two successive linear functions (softer materials, see examples given for graphite, marble, JSC-1 and gypsum) and with only one linear function for harder targets (see example given for magnetite). Other targets are not represented here but they behave similarly and all have their first shot acoustic energy between 1×10^{-3} Pa^2 s and 2×10^{-3} Pa^2 s. Normalized evolution of acoustic energy for targets that are not represented here can be found in Fig. 12 and in Fig. 15 for the first shot acoustic energy for each target. Acoustic energy for metal is not displayed in this plot but is represented in Fig. 9a.

with the ablated volume.

The evolution of the ablated volume as a function of the number of laser shots that built the crater is given in Fig. 11. The same behavior is observed for all the targets including the metals: the ablation rate is higher during a first phase lasting about 30 shots. Then it is followed by an almost constant ablation rate phase, leading to a linear increase of the volume (see also evolution of the ablated volume in linear scale in Fig. 7b). As for the evolution of the shot-to-shot ablated volume, two groups of targets can be identified in Fig.

11: targets with an ablated volume higher than 4×10^6 µm^3 after 150 shots (upper part of the figure, starting from the basalt) and a second group with targets with an ablated volume lower than 2×10^6 µm^3, that includes iron oxides, graphite and metals with the exception of lead. Notice that, due to the representation of the volume in a logarithmic scale, the evolution of the ablated volume for targets in the second group is almost flat compared to targets belonging to the first group.

Those two groups of ablated volume almost concur with the two groups of targets highlighted in Fig. 10 for the acoustic energy. Targets with a high ablated volume show a slope change in the shot-to-shot evolution of the acoustic energy whereas no slope change is seen in acoustic data for targets with a lower ablated volume, with the exception of albite and graphite. For the albite, no slope change was observed for the acoustic energy, but for this target (and also for the enstatite) the normalized standard deviation of the acoustic energy over the 150 shots is at least twice as high as other targets (see normalized acoustic energy for albite and enstatite in Fig. 12). This can be explained by the high optical penetration depth for enstatite and albite (see Table 2) leading to a less efficient laser-to-target coupling. Therefore, the shot-to-shot acoustic energy varies much more than for other targets, leading to a bias in the slope retrieval. For the graphite, a slope change around the 20th shot is noticed on acoustic data whereas the ablation volume is of the order of magnitude of iron oxide target. As was mentioned for the other metals (see section 5.1), this may be explained by the thermal penetration depth for graphite (2497 nm [37]) that is 60 times higher than its optical penetration depth (41 nm [42]). Therefore, the energy absorbed by the graphite is dissipated through heat conduction leading to a lower amount of energy partitioned to ablation. Considering its physical properties, graphite has a behavior comparable to metals.

For the first group of targets identified in Figs. 10 and 11, the softer ones, the ablation rate is high, especially during the first tens of shots: from ∼40 µm for basalt up to ∼300 µm for gypsum after only 30 shots. Thus, as the crater is growing quickly, some cavity effects rapidly reduce the laser-material interaction when the number of shots increases, leading to a rapid decrease of the acoustic energy: the plasma is more and more confined, hence denser, enhancing its shielding of the beam. A smaller fraction of the laser energy reaches the target, weakening the shock-wave. In addition to that, and to a lesser extent, the laser no longer impacts a flat surface orthogonal to the beam, but instead is incident on tilted crater walls, leading to a geometric reduction of the irradiance deposited when the laser is fired inside a cavity. After a given depth that may depend on the nature of the target, the plasma shielding may have reached a maximum and only the geometric reduction of the laser-material coupling decreases the acoustic energy, possibly explaining the slope change seen on acoustic data. For the second group of targets, the harder ones, the laser crater is shallow (less than $\sim$10 µm after 30 shots) likely leading to an almost constant shot-to-shot plasma shielding. Variations of plasma shielding with the number of shot cannot be seen in acoustic data. Only changes of surface properties and crater formation downgrade the laser-target interaction and are responsible for the slight decrease of the acoustic energy.

These assumptions regarding the plasma parameters can be compared with the LIBS optical spectrum intensity itself. Fig. 12 compares the shot-to-shot evolution of the acoustic energy with the evolution of the LIBS spectrum intensity in the VNIR range. Both values are normalized to corresponding values for the first shot. Targets are arranged with respect to the ablated volume: the two first rows in Fig. 12 group together targets with a high ablated volume with the addition of the enstatite for which the volume was impossible to measure. The last row puts together targets with a lower ablated volume: iron oxides and graphite.

As was already observed for samples targeted under Earth atmosphere, the evolution of the optical spectrum intensity differs relative to that of the acoustic energy depending on the amount of material ablated from each target. For targets which have high ablation rates (the two first rows in Fig. 12), the acoustic energy decreases, whereas the LIBS spectrum intensity increases. This increase may indicate a denser plasma as it is more and more confined as the cavity grows. Moreover, after 150 shots, the difference between the normalized LIBS optical spectrum intensity and the normalized acoustic energy is all the more important as

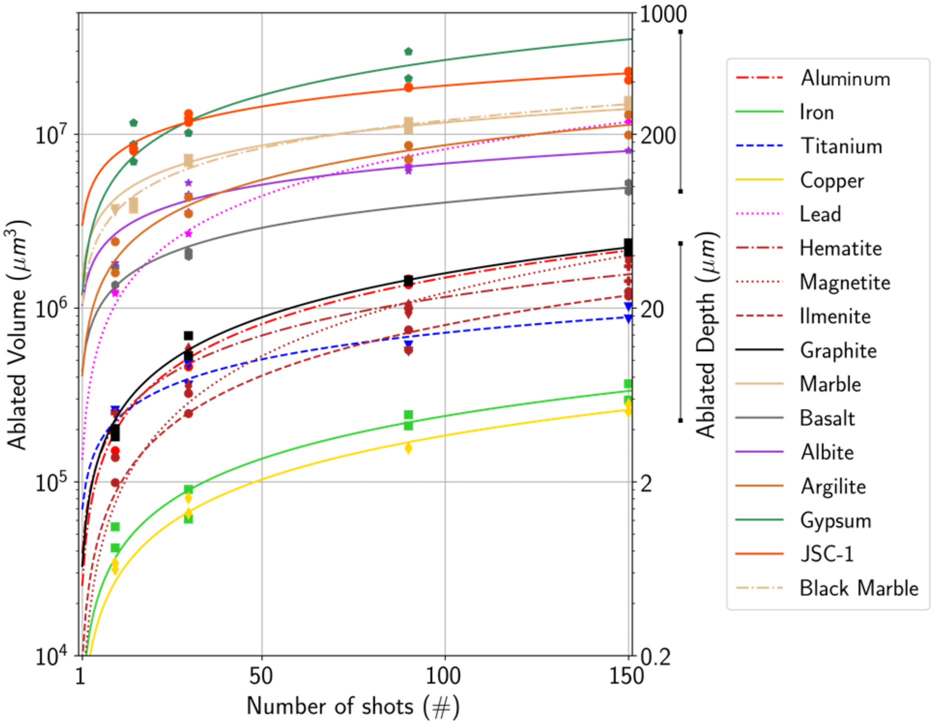

Figure 11: Evolution of the ablated volume (and depth) as a function of the number of shots for 17 of the 18 targets tested (including metals). There are 2 (or 3) repeated points per target for a given number of shots that created the crater. The volume for enstatite is not represented because of poor measurements. Measurement uncertainties are not represented as they are barely visible for volumes higher than 1×10^5 µm^3. They are displayed for metals in Fig. 9b. Details on measurement uncertainty on the volume are provided in Section 3.3. Points for all other targets are best fitted with a power law ax^b (colored lines). Vertical bars on the right of the figure show the two groups of targets discussed in the text with respect to the ablated volume.

the ablated volume is high. For instance, the basalt is the target belonging to this group that has the lowest measured ablated volume. It is also the target from this group that presents the smallest gap between the normalized acoustic energy and the normalized LIBS optical spectrum intensity. For gypsum, the LIBS spectrum intensity starts decreasing after 50 shots. This effect, which was also observed under Earth atmosphere, is likely due to the crater shape anomaly highlighted in Fig. 8. After 50 shots the laser may ablate torn walls and some matter that is loosely consolidated or collapsed at the bottom of the crater, resulting in a more rapid loss of coupling for this target. For targets with a low ablation rate (last row in Fig. 12), the LIBS optical spectrum intensity seems to follow the same variation as the acoustic energy. As laser craters formed in these targets are shallow, no cavity-induced effects are seen in the LIBS optical trends.

As a conclusion, the evolution of the LIBS spectrum can be explained by changes of plasma properties when it is produced inside a cavity. This explanation is consistent with the hypothesis made above stating that the shot-to-shot decrease of the acoustic energy is a consequence of the growth of the laser-induced cavity. Therefore, the next section applies these findings to the study of the Martian targets to be analyzed with SuperCam on Mars.

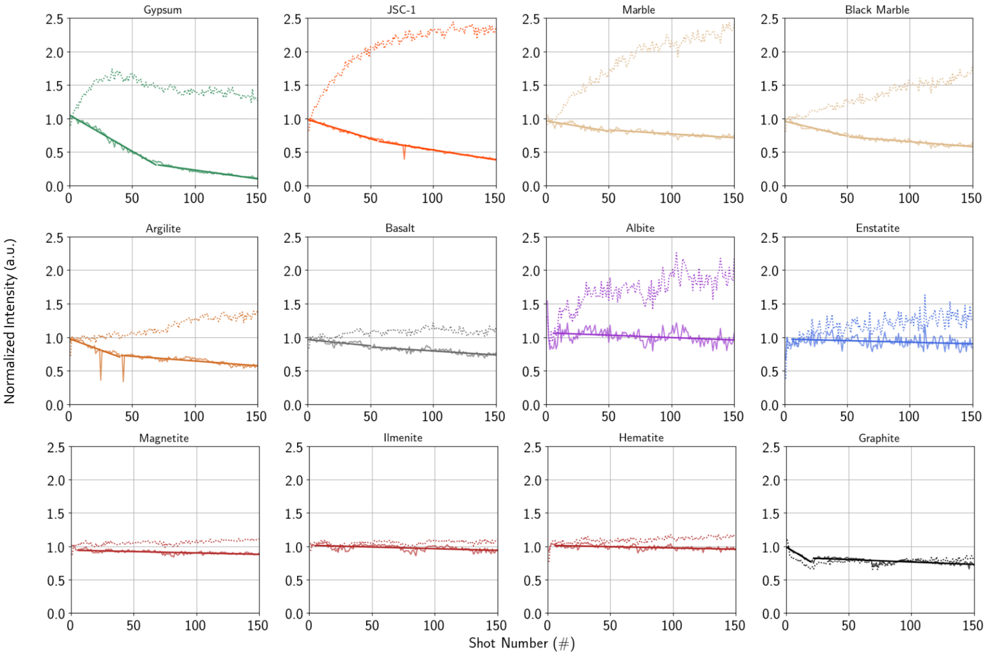

Figure 12: Shot-to-shot evolution of the acoustic energy normalized by the first shot (solid line) compared with the evolution of the normalized LIBS spectrum intensity in the VNIR range, including the continuum (dotted line). Targets that have a high ablated volume are grouped in the two first rows, with the addition of the enstatite for which the ablated volume measurement was impossible but that presents an increasing continuum. The last row groups targets that are shown to have a lower ablation rate. The portions of linear functions that fit the evolution of the acoustic energy is also represented.

6. The acoustics as a support to LIBS investigations on Mars

The combined study of the acoustic energy and the ablated volume has shown that the decrease of the former is a tracer of the ablated volume: the softer the target, the higher the ablated volume and the faster the decrease of the acoustic energy. Hence, tracking the acoustic energy along a LIBS burst can give information about both the target hardness and the ablated volume.

6.1. Inferring target hardness

It has been observed that the shot-to-shot acoustic energy can be represented by portions of linear functions, two for softer targets and only one for harder materials. Linear functions are expressed with the following expression $E = E_0\,(1 - m)$ with m given as the normalized linear decay rate. In order to be as close as the usual operational conditions of SuperCam on Mars, for each target ,the linear function is fitted only over the 30 first shots (typical number of shots performed on Mars). Only for the graphite whose slope change in the acoustic energy occurs before the 30th shot, the linear function is fitted from the first shot up to the transition (20th shot). This linear decay rate m of the acoustic energy is represented as a function of the Vickers hardness measured for each target in Fig. 13. It is also compared with the same measurements under Earth atmosphere extracted from our previous study for gypsum, the JSC-1 pellet, black marble and magnetite. This figure shows that the decay rate of the acoustic energy is a decreasing function of the Vickers hardness. This coefficient, expressed in shot^{-1} is independent from the absolute amplitude of the acoustic energy but also almost the same for an ablation under Earth atmosphere and Mars atmosphere. Only points for the enstatite (blue square) and the albite (purple star) do not follow the same trend as other targets and have a larger dispersion. Indeed, the relatively high standard deviation of the acoustic energy for these two targets, likely due to high optical penetration depth, may lead to a bias in slope retrieval. For this type of targets, there is a risk of misinterpreting the data that could be evaluated with the dispersion of the acoustic energy along a burst. It may also be difficult to distinguish the harder materials with this method but only infer that they have a Vickers hardness higher than 500.

However, Fig. 13 confirms that the decrease rate of the acoustic energy can be used to estimate rock hardness at remote distance on Mars. It extends under Mars atmosphere and with a larger set of targets our previous results obtained under Earth atmosphere. Moreover, as the linear decrease of the acoustic energy is extracted from a fit from the first shot of a burst to a slope change in data, if it occurs, it does not require long sequence of shots. Therefore, on Mars with SuperCam, it will be possible to estimate hardness on the majority of targets as during the 8 years of activity on Mars, most of the ChemCam targets were fired with bursts of only 30 shots.

It should be noted that other approaches exist to estimate target hardness that are only based on the LIBS spectrum: the ratio of ionic to atomic emission lines [66, 67] but also the plasma temperature [68, 69] were shown to linearly correlate with the hardness of selected targets. This is likely the result of a faster shock-wave for the harder materials that leads to a more ionized plasma [70]. The approach chosen in our study only relies on the acoustic energy.

Looking at the results with the Mars Science Laboratory rover at Gale crater, each geological formation can cover a large area (km^2) and so a Mars rover may travel for many months in the same formation. However, that formation can have variations in hardness that can affect drilling capabilities and which are also of geological interest. These hardness variations can occur due to changes in pore-filling cements of sediments and/or alteration. Vera Rubin ridge, which formed through deflation of softer surrounding sediments, is one example [71, 72], where the ridge presented difficulties in drilling, and the ridge's physical properties were also of strong scientific interest [73]. In our study, we investigated a group of diverse rock and mineral types. An investigation using various samples that are all from the same sedimentary formation but have different hardness values may show a much tighter correlation than that seen in Fig. 13. Such a study may provide a better estimate of the accuracy of the hardness values that can be determined from SuperCam in a realistic setting.

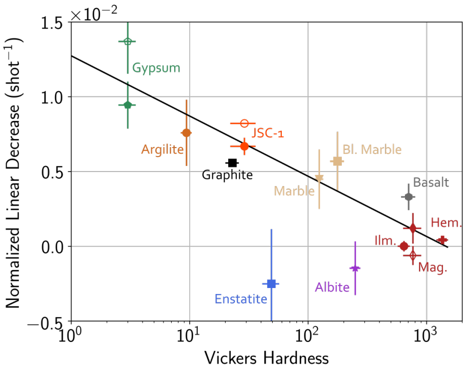

Figure 13: Linear decay rate of the acoustic energy measured for the 12 minerals and rocks tested in this study under Mars atmosphere (filled markers) as a function of the Vickers hardness measured for each material. It is compared with linear decay rate computed for the same gypsum, JSC-1, black marble and magnetite whose data are extracted from our previous study under Earth atmosphere (unfilled markers). Linear decay rate is computed by fitting a linear function over the 30 first shots for bursts of 30, 90 and 150 shots. If the slope change observed on the acoustic energy occurred before the 30th, the fit is performed up to the transition. Vertical error bars represent the standard deviations of the linear decay rates retrieved for the bursts of 30, 90 and 150 shots on each target. Horizontal error bars represent the standard deviation between the 5 hardness measurements performed per target. Marker shape and color follow the same color code than in Fig. 10. Both data sets are fitted with a straight line (solid line for Mars data, dashed line for Earth data). Hem: Hematite, Mag: Magnetite, Ilm: Ilmenite.

6.2. Estimation of the ablated volume

Our previous study under Earth atmosphere has demonstrated that the relative decrease of the acoustic energy was linearly linked with the ablated volume and that this relationship was quite independent of the target properties. For each rock and mineral tested in this study, Fig. 14 shows the acoustic energy of the last shot of the sequence that created a given crater as a function of the measured ablated volume of this crater. Acoustic energies are normalized by the first shot of the sequence. It is compared with results under Earth atmosphere [1], for the four targets that are in common between the two studies. All these data follow a linear trend confirming that the decrease of the acoustic energy can be used to estimate the ablated volume after a given amount of shots. As reported as part of the comparison with the ablation under Earth atmosphere (see section 4.4), both the excavated volumes and the acoustic energies were similar, so it makes sense that both results under Earth and Mars atmosphere follow the same trend. It can be noticed that for the graphite sample, although the acoustic energy is a linear function of the ablated volume, the acoustic energy decreases faster than for other minerals. This may be explained by the singular thermal behavior of graphite. The laser was fired perpendicular to the graphene planes that have a very high thermal conductivity [37]. Therefore heat must have been dissipated by the sides of the crater. For volumes lower than $1 \times 10^7\,\mu m^3$ the dispersion around the fitted line is larger than for higher volumes. It may be due to surface roughness that affects volume measurements in a larger extent for shallow craters than for deep ones. With SuperCam on Mars, most of the targets will be ablated with burst of 30 shots but with a laser energy greater than 24 mJ [6] that might result in deeper craters: laser-induced craters created with 30 shots on a basalt sample with the qualification model of SuperCam were 120 µm deep [7] compared to ∼40 µm with the laser used in this study. However, bursts of 150 shots or more will be possible with SuperCam to create deeper craters on specific targets.

Nevertheless, this linear relationship between the ablated volume and the acoustic energy, observed under Earth atmosphere, is confirmed and extended under Mars atmosphere for most of the rocks and minerals tested in this study. It demonstrates that the SuperCam microphone has the ability to estimate the ablated volume of LIBS targets, and consequently the crater depth. This is valuable information in order to study the chemical stratification with depth, especially to constrain the thickness of rock coatings [74]. The volume estimation would also be critical to discuss the heterogeneity of a target that presents variations in its shot-to-shot LIBS signal.

6.3. Sensitivity of the measurements expected on Mars

It was noted in Section 5 that the absolute amplitude of the acoustic energy was not the same for all the targets (see Figs. 9a for metals and 10 for other targets). Hence, one could wonder to what extend it depends on target properties or on experimental parameters. Indeed, it was also noted in Section 4 that the pressure, the laser-to-target distance, and also the focus quality play a role in the amplitude of acoustic energy. Measurements that led to results of Section 5 were subject to some variations of these parameters during the course of the experiments that are listed below, and summarized in Table 3:

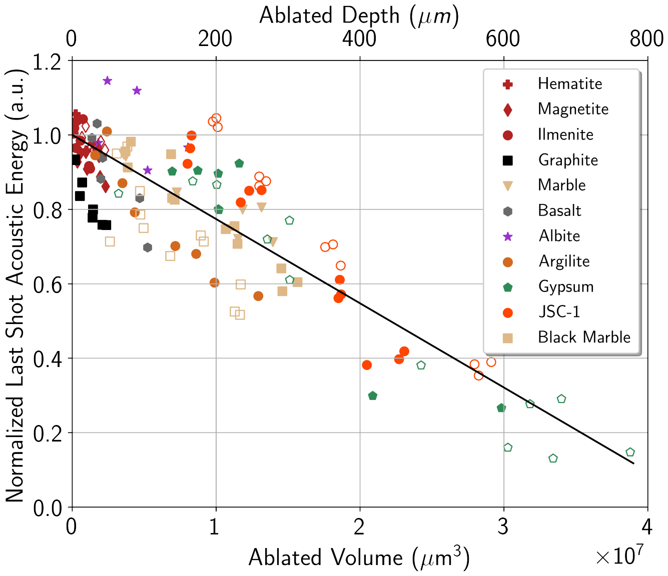

Figure 14: Normalized acoustic energy recorded at the bottom of the laser crater (*i.e.* the mean acoustic energy of the 5 last shots of the burst that created the crater) as a function of the associated crater volume (filled colored markers). Craters were created with 10, 30, 90 and 150 shots. Acoustic energies are normalized by the mean value recorded for the 5 first shots of the sequence. For each target 2 (or 3) craters were created and measured for each number of shots used. The Mars atmosphere results are compared with the same data, extracted from our previous study under Earth atmosphere for the four targets that were used for studies (gypsum, JSC-1, black marble and magnetite; unfilled markers). Mars data are fitted with a linear function $y = 1 - 2.38 \times 10^{-8} x$ (black solid line).

- Pressure inside the chamber varied from ± 0.3 mbar around 6.22 mbar between the different targets but is precisely known thanks to the pressure sensor.

- The CWL-based autofocus capability of ChemCam finds the best focus within ± 0.5% of the real distance. Considering the curves given in Fig. 5, this uncertainty on the focus (corresponding to an uncertainty of 8 mm at this working distance) gives an uncertainty on the acoustic energy of ± 20% if we rely on the magnetite and titanium curves or an uncertainty of ± 50% for the enstatite. Here we consider ± 20% of uncertainty for metal, iron oxides and also graphite that behaves the same way, and ± 50% of uncertainty for all other targets.

- The laser-to-target distance was changed slightly between targets depending on their thickness. Therefore, a variation of the optical path length of ± 10 mm leads to a variation of the acoustic energy of ± 0.5% considering the power law modeled in Fig. 6. This uncertainty is considered negligible compared to the uncertainty on the focus.

The amplitude of the acoustic energy is corrected for pressure variations based on the linear relationship determined in Fig. 4. Therefore the uncertainty on the absolute amplitude of the acoustic energy mainly originates from the uncertainty on the focus. The absolute acoustic energy recorded for all the targets and corrected for pressure variations are represented in Fig. 15. Error bars correspond to the relative uncertainty on the focus for each target. The figure shows that the graphite sample has a louder sound and its error bar does not overlap other uncertainty intervals. Following graphite, lead and iron have an intermediate acoustic energy with a small uncertainty. All other targets uncertainty intervals intersect the $1 \times 10^{-3}\,\mathrm{Pa}^2\,\mathrm{s}$ to $2 \times 10^{-3}\,\mathrm{Pa}^2\,\mathrm{s}$ acoustic energy range. As for now, the link between absolute value of the acoustic energy and target properties is not reachable with the simple model considered in this work. It should be addressed by upcoming studies.

Environmental and instrumental parameters will also vary on Mars, according to the predicted ranges defined in Table 3. The law of change of irradiance with distance for the flight-model of SuperCam was calibrated in laboratory before delivery [6]. The atmospheric pressure will be known precisely, thanks to the Mars Environmental Dynamics Analyzer (MEDA), the weather station of the *Perseverance* rover, with a precision better than 0.05 mbar [75]. Finally, unlike this study, the autofocus capability of SuperCam will rely on the Remote-Micro Imager that provides a precision more than twice as good as the CWL-based autofocus capability [6].

Therefore, in order to compare absolute acoustic energies from all the targets on Mars whatever the configuration of their sampling, the following corrections will need to be implemented:

i Correction for the decrease in irradiance with the distance: Fig 6 showed that acoustic energy is proportional to the irradiance. Acoustic data can be scaled as if the irradiance was the irradiance reached at 1.56 m (distance to the calibration targets).

ii Correction for the attenuation of acoustic waves along the sound path length: acoustic data can be scaled as if they were measured at a distance of 1.56 m based on Equation 1 and the attenuation coefficient extracted from Bass and Chambers [30]. As the attenuation coefficient depends on atmospheric pressure and temperature, *in situ* measurements from MEDA will help to better compute it.

iii Correction for background pressure variation. This can be done based on MEDA measurements.

iv Consideration of the uncertainty associated to the focus. This will provide one term in the assessment of the uncertainties. Based on the value provided in Table 3, this uncertainty will be lower on Mars than during these experiments.

7. Conclusion

Listening to laser-induced sparks produced under Earth atmosphere has shown to provide useful information on target hardness and ablated volume [1]. In an refinement of this work

Variation of Env. and Exp. Parameters	This study	Expected on Jezero Crater, Mars
Pressure	6.22 ± 0.3 mbar	Between 6 mbar and 8.5 mbar depending on the season. Diurnal variations up to ± 3% [76]
Laser-to-target Distance	1656 ± 10 mm	From 2.1 m to 7 m and 1.56 m for calibration targets [6]
Focus Quality	± 0.5% of the total distance [52].	± 0.2% of the total distance [6].

Table 3: Variation of environmental (Env.) and experimental parameters (Exp.) that occurred during this study (2nd column) and expected on Mars at the *Perseverance* landing site (3rd column). Variation of air temperature is not listed here as it was not tested in this study but it is expected to vary between 180 K and 260 K depending on the local hour and season [76]. Therefore it will have an impact of air density and sound attenuation coefficient.

and in preparation for the SuperCam LIBS investigation on Mars, the acoustic signal from the expansion of the laser plasma on metals, minerals, and rocks, was studied under controlled Mars conditions (carbon dioxide atmosphere and low pressure).

The sensitivity of the acoustic signal with respect to environmental and instrumental parameters that govern laser ablation and sound propagation was experimentally explored. On the one hand, the amplitude of the acoustic energy increases linearly with the background pressure for the range expected at the Mars 2020 *Perseverance* rover landing site. On the other hand, the laser irradiance at the target controls the intensity of the acoustic signal. The acoustic energy decreases for targets farther to the instrument, due the loss of irradiance with the optical path length (*e.g.*, poorer focusing of the laser beam at longer distances) in addition to a longer distance of attenuation of the sound as it travels back to the instrument. Furthermore, the sound is louder at best focus, and when the focal point of the telescope is moved away from the target surface, the acoustic energy drops down with the same depth of field as the LIBS optical spectrum intensity. The characterization of the dependence of the acoustic energy with respect to these parameters will be used to scale future

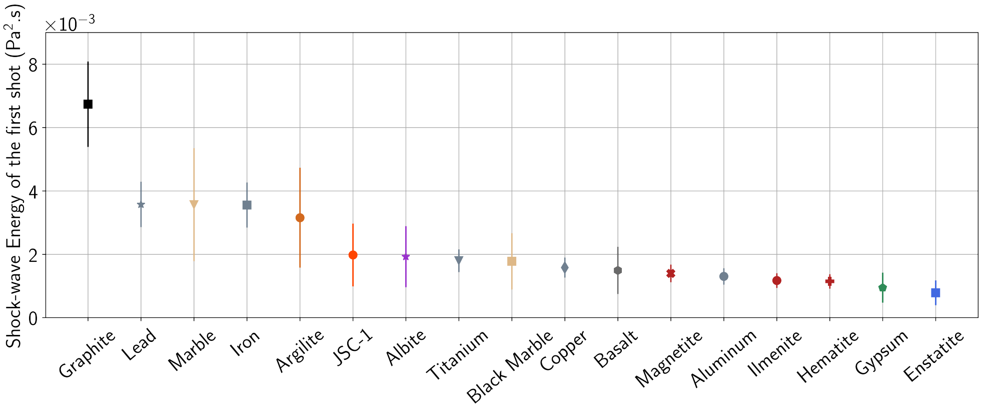

Figure 15: First shot acoustic energy recorded for each target given with error bars that correspond to the relative uncertainty on the focus (see text). All points were scaled to take into account the small difference in background pressure variation between two successive bursts of shots. Targets are sorted by decreasing acoustic energy.

Mars data and to compare acoustic signal from targets sampled under multiple configurations.

The shot-to-shot evolution of the acoustic energy is demonstrated to be intrinsically linked to the amount of ablated material and the nature of the targeted sample. For metal, the acoustic energy is almost constant over 150 shots because of a low ablated volume due to a long thermal penetration depth compared to the optical penetration depth that is responsible for energy dissipation inside the target. For other rocks and minerals, the shot-to-shot decay rate of the acoustic energy over a series of laser shots is a decreasing function of the target hardness. This information will be valuable for the *Perseverance* rover team to estimate the hardness of potential drill targets and also to track changes of material properties with laser crater depth, such as in characterizing rock coatings, if they are discovered. The ratio between the acoustic energy of the first and the last shot of a LIBS burst is seen to be a linear function of the ablated volume and depth, with the same correlation slope as the one already observed for ablation under Earth atmosphere. Indeed it was noticed that the ablation rate under Earth and Mars atmospheres are comparable.

Finally, this study highlights the potential of the microphone to complement the SuperCam LIBS investigation of rocks and soils by measuring the ablated volume and estimating the target hardness. This work also characterizes the sensitivity of the acoustic energy over a representative range of environmental parameters, instrumental configurations and target properties. The different relationships presented here will help to compare Martian data from one target to another.

Acknowledgments

This work was funded by CNES and Région Occitanie as part of a PhD thesis. We gratefully acknowledge Guy Perez and Romain Petre Bordenave from CNES for their availability with the 3D-surface profiler. Thanks are due to Jean-Claude Boulliard and the Collection de Minéraux (Sorbonne Université, Paris) for providing mineral samples. The NASA Mars Exploration Program supported some parts (ChemCam body unit, RCW participation).

References

[1] B. Chide, S. Maurice, N. Murdoch, J. Lasue, B. Bousquet, X. Jacob, A. Cousin, O. Forni, O. Gasnault, P.-Y. Meslin, J.-F. Fronton, M. Bassas-Portús, A. Cadu, A. Sournac, D. Mimoun, R. C. Wiens, Listening to laser sparks: a link between laser-induced breakdown spectroscopy, acoustic measurements and crater morphology, Spectrochimica Acta Part B: Atomic Spectroscopy 153 (2019) 50–60. URL: https://doi.org/10.1016/j.sab.2019.01.008. doi:10.1016/j.sab.2019.01.008.

[2] J.-P. Williams, Acoustic environment of the martian surface, Journal of Geophysical Research: Planets 106 (2001) 5033–5041. doi:10.1029/1999je001174.

[3] W. B. Banerdt, S. E. Smrekar, D. Banfield, D. Giardini, M. Golombek, C. L. Johnson, P. Lognonné, A. Spiga, T. Spohn, C. Perrin, S. C. Stähler, D. Antonangeli, S. Asmar, C. Beghein, N. Bowles, E. Bozdag, P. Chi, U. Christensen, J. Clinton, G. S. Collins, I. Daubar, V. Dehant, M. Drilleau, M. Fillingim, W. Folkner, R. F. Garcia, J. Garvin, J. Grant, M. Grott, J. Grygorczuk, T. Hudson, J. C. E. Irving, G. Kargl, T. Kawamura, S. Kedar, S. King, B. Knapmeyer-Endrun, M. Knapmeyer, M. Lemmon, R. Lorenz, J. N. Maki, L. Margerin, S. M. McLennan, C. Michaut, D. Mimoun, A. Mittelholz, A. Mocquet, P. Morgan, N. T. Mueller, N. Murdoch, S. Nagihara, C. Newman, F. Nimmo, M. Panning, W. T. Pike, A.-C. Plesa, S. Rodriguez, J. A. Rodriguez-Manfredi, C. T. Russell, N. Schmerr, M. Siegler, S. Stanley, E. Stutzmann, N. Teanby, J. Tromp, M. van Driel, N. Warner, R. Weber, M. Wieczorek, Initial results from the InSight mission on mars, Nature Geoscience 13 (2020) 183–189. doi:10.1038/s41561-020-0544-y.

[4] L. Martire, R. F. Garcia, L. Rolland, A. Spiga, P. Lognonné, D. Banfield, W. B. Banerdt, R. Martin, Martian infrasound: Numerical modeling and analysis of InSight's data, Journal of Geophysical Research: Planets (2020). doi:10.1029/2020je006376.

[5] J. Maki, D. Gruel, C. McKinney, M. Ravine, the ECAM Team, The mars 2020 engineering cameras and microphone on the perseverance rover: A next-generation imaging system for mars exploration, Space Science Review (submitted).

[6] S. Maurice, R. Wiens, P. Bernardi, P. Cais, S. Robinson, A. Nelson, O. Gasnault, J.-M. Reess, M. Deleuze, F. Rull, J.-A. Manrique, the SuperCam Team, The supercam instrument suite on the mars 2020 rover: Science objectives and mast-unit description, Space Science Review (submitted).

[7] R. Wiens, S. Maurice, S. Robinson, A. E. Nelson, P. Cais, P. Bernardi, R. Newell, S. Clegg, S. Sharma, S. Storms, J. Deming, D. Beckman, A. Ollila, O. Gasnault, the SuperCam Team, The supercam instrument suite on the mars 2020 rover: Body unit and combined system tests, Space Science Review (submitted).

[8] B. Chide, N. Murdoch, Y. Bury, S. Maurice, X. Jacob, J. P. Merrison, J. J. Iversen, P.-Y. Meslin, M. Bassas-Portús, A. Cadu, A. Sournac, B. Dubois, R. D. Lorenz, D. Mimoun, R. C. Wiens, Experimental

wind characterization with the SuperCam microphone under a simulated martian atmosphere, Icarus (2020). doi:10.1016/j.icarus.2020.114060.

[9] B. Chide, S. Maurice, D. Mimoun, N. Murdoch, R. Lorenz, R. Wiens, Speed of Sound Measurements on Mars and its Implications, in: 51st Lunar and Planetary Science Conference, The Woodlands, TX, United States, 2020, p. 1366.

[10] B. Campanella, S. Legnaioli, S. Pagnotta, F. Poggialini, V. Palleschi, Shock waves in laser-induced plasmas, Atoms 7 (2019) 57. doi:10.3390/atoms7020057.

[11] L. Grad, J. Možina, Acoustic in situ monitoring of excimer laser ablation of different ceramics, Applied Surface Science 69 (1993) 370–375. doi:10.1016/0169-4332(93)90536-k.

[12] N. Murdoch, B. Chide, J. Lasue, A. Cadu, A. Sournac, M. Bassas-Portús, X. Jacob, J. Merrison, J. Iversen, C. Moretto, C. Velasco, L. Parès, A. Hynes, V. Godiver, R. Lorenz, P. Cais, P. Bernardi, S. Maurice, R. Wiens, D. Mimoun, Laser-induced breakdown spectroscopy acoustic testing of the mars 2020 microphone, Planetary and Space Science 165 (2019) 260–271. doi:10.1016/j.pss.2018.09.009.

[13] N. L. Lanza, A. M. Ollila, A. Cousin, R. C. Wiens, S. Clegg, N. Mangold, N. Bridges, D. Cooper, M. Schmidt, J. Berger, R. Arvidson, N. Melikechi, H. E. Newsom, R. Tokar, C. Hardgrove, A. Mezzacappa, R. S. Jackson, B. Clark, O. Forni, S. Maurice, M. Nachon, R. B. Anderson, J. Blank, M. Deans, D. Delapp, R. Léveillé, R. McInroy, R. Martinez, P.-Y. Meslin, P. Pinet, Understanding the signature of rock coatings in laser-induced breakdown spectroscopy data, Icarus 249 (2015) 62–73. doi:10.1016/j.icarus.2014.05.038.

[14] J. M. Vadillo, J. M. F. Romero, C. Rodríguez, J. J. Laserna, Effect of plasma shielding on laser ablation rate of pure metals at reduced pressure, Surface and Interface Analysis 27 (1999) 1009–1015. doi:10.1002/(sici)1096-9918(199911)27:11<1009::aid-sia670>3.0.co;2-2.

[15] E. Manikanta, L. V. Kumar, P. Venkateshwarlu, C. Leela, P. P. Kiran, Effect of pulse duration on the acoustic frequency emissions during the laser-induced breakdown of atmospheric air, Applied Optics 55 (2016) 548. doi:10.1364/ao.55.000548.

[16] E. Manikanta, L. V. Kumar, C. Leela, P. P. Kiran, Effect of laser intensity on temporal and spectral features of laser generated acoustic shock waves: ns versus ps laser pulses, Applied Optics 56 (2017) 6902. doi:10.1364/ao.56.006902.

[17] C. Stauter, P. Gérard, J. Fontaine, T. Engel, Laser ablation acoustical monitoring, Applied Surface Science 109-110 (1997) 174–178. doi:10.1016/s0169-4332(96)00655-1.

[18] S. Conesa, S. Palanco, J. Laserna, Acoustic and optical emission during laser-induced plasma formation, Spectrochimica Acta Part B: Atomic Spectroscopy 59 (2004) 1395–1401. doi:10.1016/j.sab.2004.06.004.

[19] X. Zeng, X. Mao, S. S. Mao, J. H. Yoo, R. Greif, R. E. Russo, Laser–plasma interactions in fused silica cavities, Journal of Applied Physics 95 (2004) 816–822. doi:10.1063/1.1635990.

[20] C. Porneala, D. A. Willis, Observation of nanosecond laser-induced phase explosion in aluminum, Applied Physics Letters 89 (2006) 211121. doi:10.1063/1.2393158.

[21] D. A. Cremers, F.-Y. Yueh, J. P. Singh, H. Zhang, Laser-Induced Breakdown Spectroscopy, Elemental Analysis, American Cancer Society, 2012. doi:10.1002/9780470027318.a0708.pub2.

[22] C. T. Walters, A. H. Clauer, Transient reflectivity behavior of pure aluminum at 10.6 microns, Applied Physics Letters 33 (1978) 713–715. doi:10.1063/1.90511.

[23] A. Bogaerts, Z. Chen, R. Gijbels, A. Vertes, Laser ablation for analytical sampling: what can we learn from modeling?, Spectrochimica Acta Part B: Atomic Spectroscopy 58 (2003) 1867–1893. doi:10.1016/j.sab.2003.08.004.

[24] A. Fau, O. Beyssac, M. Gauthier, P. Meslin, A. Cousin, K. Benzerara, S. Bernard, J. Boulliard, O. Gasnault, O. Forni, R. Wiens, M. Morand, P. Rosier, Y. Garino, S. Pont, S. Maurice, Pulsed laser-induced heating of mineral phases: Implications for laser-induced breakdown spectroscopy combined with raman spectroscopy, Spectrochimica Acta Part B: Atomic Spectroscopy 160 (2019) 105687. doi:10.1016/j.sab.2019.105687.

[25] M. A. Shannon, A simplified cavity analysis for estimating energy coupling during laser ablation and drilling of solids – theory, Applied Surface Science 127-129 (1998) 218–225. doi:10.1016/s0169-4332(97)00635-1.

[26] G. Taylor, The formation of a blast wave by a very intense explosion i. theoretical discussion, Proceedings of the Royal Society of London. Series A. Mathematical and Physical Sciences 201 (1950) 159–174. doi:10.1098/rspa.1950.0049.

[27] Y. Zel'dovich, Y. Raizer, Physics of Shock Waves and High-Temperature Hydrodynamic Phenomena, Elsevier, 1967. doi:10.1016/b978-0-12-395672-9.x5001-2.

[28] S. S. Harilal, G. V. Miloshevsky, P. K. Diwakar, N. L. LaHaye, A. Hassanein, Experimental and computational study of complex shockwave dynamics in laser ablation plumes in argon atmosphere, Physics of Plasmas 19 (2012) 083504. doi:10.1063/1.4745867.

[29] H. E. Bass, L. C. Sutherland, J. Piercy, L. Evans, Absorption of sound by the atmosphere, in: Physical acoustics: Principles and methods, volume 17, 1984, pp. 145–232.

[30] H. E. Bass, J. P. Chambers, Absorption of sound in the martian atmosphere, The Journal of the Acoustical Society of America 109 (2001) 3069–3071. doi:10.1121/1.1365424.

[31] A. K. Knight, N. L. Scherbarth, D. A. Cremers, M. J. Ferris, Characterization of laser-induced breakdown spectroscopy (LIBS) for application to space exploration, Applied Spectroscopy 54 (2000) 331–340. doi:10.1366/0003702001949591.

[32] W. Rapin, P.-Y. Meslin, S. Maurice, R. Wiens, D. Laporte, B. Chauviré, O. Gasnault, S. Schröder, P. Beck, S. Bender, O. Beyssac, A. Cousin, E. Dehouck, C. Drouet, O. Forni, M. Nachon, N. Melikechi, B. Rondeau, N. Mangold, N. Thomas, Quantification of water content by laser induced breakdown

spectroscopy on mars, Spectrochimica Acta Part B: Atomic Spectroscopy 130 (2017) 82–100. doi:10.1016/j.sab.2017.02.007.

[33] T. Dequaire, P.-Y. Meslin, P. Beck, M. Jaber, A. Cousin, W. Rapin, J. Lasne, O. Gasnault, S. Maurice, A. Buch, C. Szopa, P. Coll, Analysis of carbon and nitrogen signatures with laser-induced breakdown spectroscopy: the quest for organics under mars-like conditions, Spectrochimica Acta Part B: Atomic Spectroscopy 131 (2017) 8–17. doi:10.1016/j.sab.2017.02.015.

[34] W. Rapin, P.-Y. Meslin, S. Maurice, D. Vaniman, M. Nachon, N. Mangold, S. Schröder, O. Gasnault, O. Forni, R. Wiens, G. Martínez, A. Cousin, V. Sautter, J. Lasue, E. Rampe, D. Archer, Hydration state of calcium sulfates in gale crater, mars: Identification of bassanite veins, Earth and Planetary Science Letters 452 (2016) 197–205. doi:10.1016/j.epsl.2016.07.045.

[35] E. Rampe, D. Ming, D. Blake, T. Bristow, S. Chipera, J. Grotzinger, R. Morris, S. Morrison, D. Vaniman, A. Yen, C. Achilles, P. Craig, D. D. Marais, R. Downs, J. Farmer, K. Fendrich, R. Gellert, R. Hazen, L. Kah, J. Morookian, T. Peretyazhko, P. Sarrazin, A. Treiman, J. Berger, J. Eigenbrode, A. Fairén, O. Forni, S. Gupta, J. Hurowitz, N. Lanza, M. Schmidt, K. Siebach, B. Sutter, L. Thompson, Mineralogy of an ancient lacustrine mudstone succession from the murray formation, gale crater, mars, Earth and Planetary Science Letters 471 (2017) 172–185. doi:10.1016/j.epsl.2017.04.021.

[36] R. Noll, Evaporation and plasma generation, in: Laser-Induced Breakdown Spectroscopy, Springer Berlin Heidelberg, 2011, pp. 75–82. doi:10.1007/978-3-642-20668-9_5.

[37] D. R. Lide, CRC Handbook of chemistry and physics, 84th ed., CRC Press, 2003.

[38] K. Horai, G. Simmons, Thermal conductivity of rock-forming minerals, Earth and Planetary Science Letters 6 (1969) 359–368. doi:10.1016/0012-821x(69)90186-1.

[39] D. W. Waples, J. S. Waples, A review and evaluation of specific heat capacities of rocks, minerals, and subsurface fluids. part 1: Minerals and nonporous rocks, Natural Resources Research 13 (2004) 97–122. doi:10.1023/b:narr.0000032647.41046.e7.

[40] M. Querry, Optical Constants, Contractor Report CRDC-CR-85034, University of Missouri, 1985.

[41] S. Li, L. Li, Radiative transfer modeling for quantifying lunar surface minerals, particle size, and submicroscopic metallic fe, Journal of Geophysical Research 116 (2011). doi:10.1029/2011je003837.

[42] A. B. Djurišić, E. H. Li, Optical properties of graphite, Journal of Applied Physics 85 (1999) 7404–7410. doi:10.1063/1.369370.

[43] M. L. Linvill, J. W. Vandersande, R. O. Pohl, Thermal conductivity of feldspars, Bulletin de Minéralogie 107 (1984) 521–527. doi:10.3406/bulmi.1984.7781.

[44] E. Sklute, T. Hiroi, C. Pieters, R. Milliken, T. Glotch, M. Parente, M. Dyar, Preliminary VNIR ptical Constants of Bytownite using Radiative Transfer Theory, in: 47th Lunar and Planetary Science Conference, The Woodlands, TX, United States, 2016, p. 2147.

[45] B. W. Denevi, P. G. Lucey, E. J. Hochberg, D. Steutel, Near-infrared optical constants of pyroxene

as a function of iron and calcium content, Journal of Geophysical Research 112 (2007). doi:10.1029/2006je002802.

[46] J. Côté, J.-M. Konrad, Thermal conductivity of base-course materials, Canadian Geotechnical Journal 42 (2005) 61–78. doi:10.1139/t04-081.

[47] L. Eppelbaum, I. Kutasov, A. Pilchin, Thermal properties of rocks and density of fluids, in: Lecture Notes in Earth System Sciences, Springer Berlin Heidelberg, 2014, pp. 99–149. doi:10.1007/978-3-642-34023-9_2.

[48] J. R. Johnson, W. M. Grundy, Visible/near-infrared spectra and two-layer modeling of palagonite-coated basalts, Geophysical Research Letters 28 (2001) 2101–2104. doi:10.1029/2000gl012669.

[49] C. C. Allen, K. M. Jager, R. V. Morris, D. J. Lindstrom, M. M. Lindstrom, J. P. Lockwood, JSC MARS-1: A martian soil simulant, in: Space 98, American Society of Civil Engineers, 1998. doi:10.1061/40339(206)54.

[50] S. Le Mouélic, O. Gasnault, K. Herkenhoff, N. Bridges, Y. Langevin, N. Mangold, S. Maurice, R. Wiens, P. Pinet, H. Newsom, R. Deen, J. Bell, J. Johnson, W. Rapin, B. Barraclough, D. Blaney, L. Deflores, J. Maki, M. Malin, R. Pérez, M. Saccoccio, The ChemCam remote micro-imager at gale crater: Review of the first year of operations on mars, Icarus 249 (2015) 93–107. doi:10.1016/j.icarus.2014.05.030.

[51] A. Cousin, S. Maurice, Y. Parot, Y. Michel, N. Le Roch, J. Dalmau, L. Pares, R. Perez, A. Cros, R. Wiens, ChemCam (MSL) Autofocus Capabilities, in: 40th Lunar and Planetary Science Conference, The Woodlands, TX, United States, 2009, p. 1684.

[52] S. Maurice, R. C. Wiens, M. Saccoccio, B. Barraclough, O. Gasnault, O. Forni, N. Mangold, D. Baratoux, S. Bender, G. Berger, J. Bernardin, M. Berthé, N. Bridges, D. Blaney, M. Bouyé, P. Caïs, B. Clark, S. Clegg, A. Cousin, D. Cremers, A. Cros, L. DeFlores, C. Derycke, B. Dingler, G. Dromart, B. Dubois, M. Dupieux, E. Durand, L. d'Uston, C. Fabre, B. Faure, A. Gaboriaud, T. Gharsa, K. Herkenhoff, E. Kan, L. Kirkland, D. Kouach, J.-L. Lacour, Y. Langevin, J. Lasue, S. Le Mouélic, M. Lescure, E. Lewin, D. Limonadi, G. Manhès, P. Mauchien, C. McKay, P.-Y. Meslin, Y. Michel, E. Miller, H. E. Newsom, G. Orttner, A. Paillet, L. Parès, Y. Parot, R. Pérez, P. Pinet, F. Poitrasson, B. Quertier, B. Sallé, C. Sotin, V. Sautter, H. Séran, J. J. Simmonds, J.-B. Sirven, R. Stiglich, N. Striebig, J.-J. Thocaven, M. J. Toplis, D. Vaniman, The chemcam instrument suite on the mars science laboratory (msl) rover: Science objectives and mast unit description, Space Science Reviews 170 (2012) 95–166. doi:10.1007/s11214-012-9912-2.

[53] Y. Lu, Y. Lee, M. Hong, T. Low, Acoustic wave monitoring of cleaning and ablation during excimer laser interaction with copper surfaces, Applied Surface Science 119 (1997) 137 – 146. doi:https://doi.org/10.1016/S0169-4332(97)00188-8.

[54] S. Palanco, J. Laserna, Spectral analysis of the acoustic emission of laser-produced plasmas, Applied Optics 42 (2003) 6078. doi:10.1364/ao.42.006078.

[55] A. Hrdlička, L. Zaorálková, M. Galiová, T. Čtvrtníčková, V. Kanický, V. Otruba, K. Novotný, P. Krásenský, J. Kaiser, R. Malina, K. Páleníková, Correlation of acoustic and optical emission signals produced at 1064 and 532 nm laser-induced breakdown spectroscopy (LIBS) of glazed wall tiles, Spectrochimica Acta Part B: Atomic Spectroscopy 64 (2009) 74–78. doi:10.1016/j.sab.2008.10.043.

[56] R. Wiens, S. Maurice, J. Lasue, O. Forni, R. Anderson, S. Clegg, S. Bender, D. Blaney, B. Barraclough, A. Cousin, L. Deflores, D. Delapp, M. Dyar, C. Fabre, O. Gasnault, N. Lanza, J. Mazoyer, N. Melikechi, P.-Y. Meslin, H. Newsom, A. Ollila, R. Perez, R. Tokar, D. Vaniman, Pre-flight calibration and initial data processing for the ChemCam laser-induced breakdown spectroscopy instrument on the mars science laboratory rover, Spectrochimica Acta Part B: Atomic Spectroscopy 82 (2013) 1–27. doi:10.1016/j.sab.2013.02.003.

[57] D. Banfield, A. Spiga, C. Newman, F. Forget, M. Lemmon, R. Lorenz, N. Murdoch, D. Viudez-Moreiras, J. Pla-Garcia, R. F. Garcia, P. Lognonné, Özgür Karatekin, C. Perrin, L. Martire, N. Teanby, B. V. Hove, J. N. Maki, B. Kenda, N. T. Mueller, S. Rodriguez, T. Kawamura, J. B. McClean, A. E. Stott, C. Charalambous, E. Millour, C. L. Johnson, A. Mittelholz, A. Määttänen, S. R. Lewis, J. Clinton, S. C. Stähler, S. Ceylan, D. Giardini, T. Warren, W. T. Pike, I. Daubar, M. Golombek, L. Rolland, R. Widmer-Schnidrig, D. Mimoun, É. Beucler, A. Jacob, A. Lucas, M. Baker, V. Ansan, K. Hurst, L. Mora-Sotomayor, S. Navarro, J. Torres, A. Lepinette, A. Molina, M. Marin-Jimenez, J. Gomez-Elvira, V. Peinado, J.-A. Rodriguez-Manfredi, B. T. Carcich, S. Sackett, C. T. Russell, T. Spohn, S. E. Smrekar, W. B. Banerdt, The atmosphere of mars as observed by InSight, Nature Geoscience 13 (2020) 190–198. doi:10.1038/s41561-020-0534-0.

[58] B. Chide, S. Maurice, B. Bousquet, J. Jacob, D. Mimoun, N. Murdoch, A. Cousin, G. David, J. Lasue, P.-Y. Meslin, R. Wiens, Focusing a Laser Induced Breakdown Spectroscopy (LIBS) telescope with a Microphone, in: 50st Lunar and Planetary Science Conference, The Woodlands, TX, United States, 2019, p. 2296.

[59] L. Peret, O. Gasnault, R. Dingler, Y. Langevin, S. Bender, D. Blaney, S. Clegg, C. Clewans, D. Delapp, C. M. Donny, S. Johnstone, C. Little, E. Lorigny, R. McInroy, S. Maurice, N. Mittal, B. Pavri, R. Perez, R. C. Wiens, C. Yana, Restoration of the autofocus capability of the ChemCam instrument onboard the curiosity rover, in: SpaceOps 2016 Conference, American Institute of Aeronautics and Astronautics, 2016. doi:10.2514/6.2016-2539.

[60] W. Rapin, Hydratation de la surface de Mars partir des donnes du rover Curiosity, Ph.D. thesis, cole doctorale Sciences de lunivers, de lenvironnement et de lespace (Toulouse), 2017.

[61] Y. Iida, Effects of atmosphere on laser vaporization and excitation processes of solid samples, Spectrochimica Acta Part B: Atomic Spectroscopy 45 (1990) 1353–1367. doi:10.1016/0584-8547(90)80188-o.

[62] P.-Y. Meslin, J. R. Johnson, O. Forni, P. Beck, A. Cousin, J. Bridges, W. Rapin, B. Cohen, H. Newsom,

V. Sautter, E. Lewin, M. Nachon, R. C. Wiens, V. Payré, O. Gasnault, S. Maurice, A. G. Fairén, S. Schröder, N. Mangold, N. Thomas, Egg Rock Encounter: Analysis of an Iron-Nickel Meteorite Found in Gale Crater by Curiosity, in: 48th Lunar and Planetary Science Conference, The Woodlands, TX, United States, 2017, p. 2258.

[63] J.-A. Manrique, G. Lopez-Reyes, A. Cousin, F. Rull, S. Maurice, R. Wiens, M. Madsen, J. Madariaga, O. Gasnault, the SuperCam Team, Supercam calibration targets: Design and development, Space Science Review (submitted).

[64] S. Preuss, A. Demchuk, M. Stuke, Sub-picosecond UV laser ablation of metals, Applied Physics A Materials Science & Processing 61 (1995) 33–37. doi:10.1007/bf01538207.

[65] Y. F. Lu, M. H. Hong, S. J. Chua, B. S. Teo, T. S. Low, Audible acoustic wave emission in excimer laser interaction with materials, Journal of Applied Physics 79 (1996) 2186–2191. doi:10.1063/1.361182.

[66] Z. Abdel-Salam, A. Galmed, E. Tognoni, M. Harith, Estimation of calcified tissues hardness via calcium and magnesium ionic to atomic line intensity ratio in laser induced breakdown spectra, Spectrochimica Acta Part B: Atomic Spectroscopy 62 (2007) 1343–1347. doi:10.1016/j.sab.2007.10.033.

[67] Z. Abdel-Salam, M. Abdelhamid, S. M. Khalil, M. A. Harith, M. A. Harith, LIBS new application: Determination of metallic alloys surface hardness, in: AIP Conference Proceedings, AIP, 2009. doi:10.1063/1.3250114.

[68] S. M. Aberkane, A. Bendib, K. Yahiaoui, S. Boudjemai, S. Abdelli-Messaci, T. Kerdja, S. Amara, M. Harith, Correlation between fe v c alloys surface hardness and plasma temperature via LIBS technique, Applied Surface Science 301 (2014) 225–229. doi:10.1016/j.apsusc.2014.02.046.

[69] H. Sattar, H. Ran, W. Ding, M. Imran, M. Amir, H. Ding, An approach of stand-off measuring hardness of tungsten heavy alloys using LIBS, Applied Physics B 126 (2019). doi:10.1007/s00340-019-7355-0.

[70] K. Tsuyuki, S. Miura, N. Idris, K. H. Kurniawan, T. J. Lie, K. Kagawa, Measurement of concrete strength using the emission intensity ratio between ca(II) 396.8 nm and ca(i) 422.6 nm in a nd:YAG laser-induced plasma, Applied Spectroscopy 60 (2006) 61–64. doi:10.1366/000370206775382668.

[71] J. Frydenvang, N. Mangold, R. C. Wiens, A. A. Fraeman, L. A. Edgar, C. Fedo, J. L'Haridon, C. C. Bedford, S. Gupta, J. P. Grotzinger, J. C. Bridges, B. C. Clark, E. B. Rampe, O. Gasnault, S. Maurice, P. J. Gasda, N. L. Lanza, A. M. Olilla, P.-Y. Meslin, V. Payré, F. Calef, M. Salvatore, C. H. House, The chemostratigraphy of the murray formation and role of diagenesis at vera rubin ridge in gale crater, mars, as observed by the ChemCam instrument, Journal of Geophysical Research: Planets (2020). doi:10.1029/2019je006320.

[72] G. David, A. Cousin, O. Forni, P.-Y. Meslin, E. Dehouck, N. Mangold, J. L'Haridon, W. Rapin, O. Gasnault, J. Johnson, A. Ollila, A. Newell, R. Wiens, S. Maurice, M. Salvatore, Analyses of high-iron sedimentary bedrock and diagenetic features observed with chemcam at vera rubin ridge, gale crater, mars: calibration and characterization, Journal of Geophysical Research: Planets (submitted).

[73] A. Fraeman, L. Edgar, E. Rampe, L. Thompson, J. Frydenvang, C. Fedo, J. Catalano, W. Dietrich, T. Gabriel, J. Grotzinger, J. L'Haridon, N. Mangold, V. Sun, C. House, A. Bryk, C. Hardgrove, S. Czarnecki, K. Stack, A. Vasavada, R. Morris, R. Arvidson, S. Banham, K. Bennett, J. Bridges, C. Edwards, W. Fischer, V. Fox, S. Gupta, B. Horgan, S. Jacob, J. Johnson, S. Johnson, D. Rubin, M. Salvatore, S. Schwenzer, K. Siebach, N. Stein, S. Turner, D. Wellington, R. Wiens, A. Williams, G. Wong, The origin of vera rubin ridge, gale crater, mars: Summary and synthesis of curiositys exploration campaign, Journal of Geophysical Research: Planets (submitted).

[74] N. Lanza, B. Chide, S. Clegg, E. Dauson, O. Forni, C. Larmat, A. Reyes-Newell, J. Ten Cate, , R. Wiens, S. Maurice, Listening for Rock Coating on Mars: Using Acoustic Signals from Laser-Induced Breakdown Spectroscopy to Identify Surface Coatings and Layers, in: 51st Lunar and Planetary Science Conference, The Woodlands, TX, United States, 2020, p. 2807.

[75] J. Rodriguez-Manfredi, M. de la Torre Juarez, the MEDA Team, The mars environmental dynamics analyzer meda. a suite of environmental sensors for the mars 2020 mission, Space Science Review (submitted).

[76] C. Newmann, M. de la Torre Juarez, J. Pla-Garcia, T. Bertrand, M. Kahre, R. Wilson, F. Daerden, L. Neary, S. Lewis, F. Forget, A. Spiga, R. Sullivan, M. Richardson, A. Sanchez-Lavega, D. Viudez-Moreiras, B. Chide, J. Rodrigez-Manfredi, Multi-model meteorological and aeolian predictions for mars 2020 and the jezero crater region, Space Science Review (submitted).

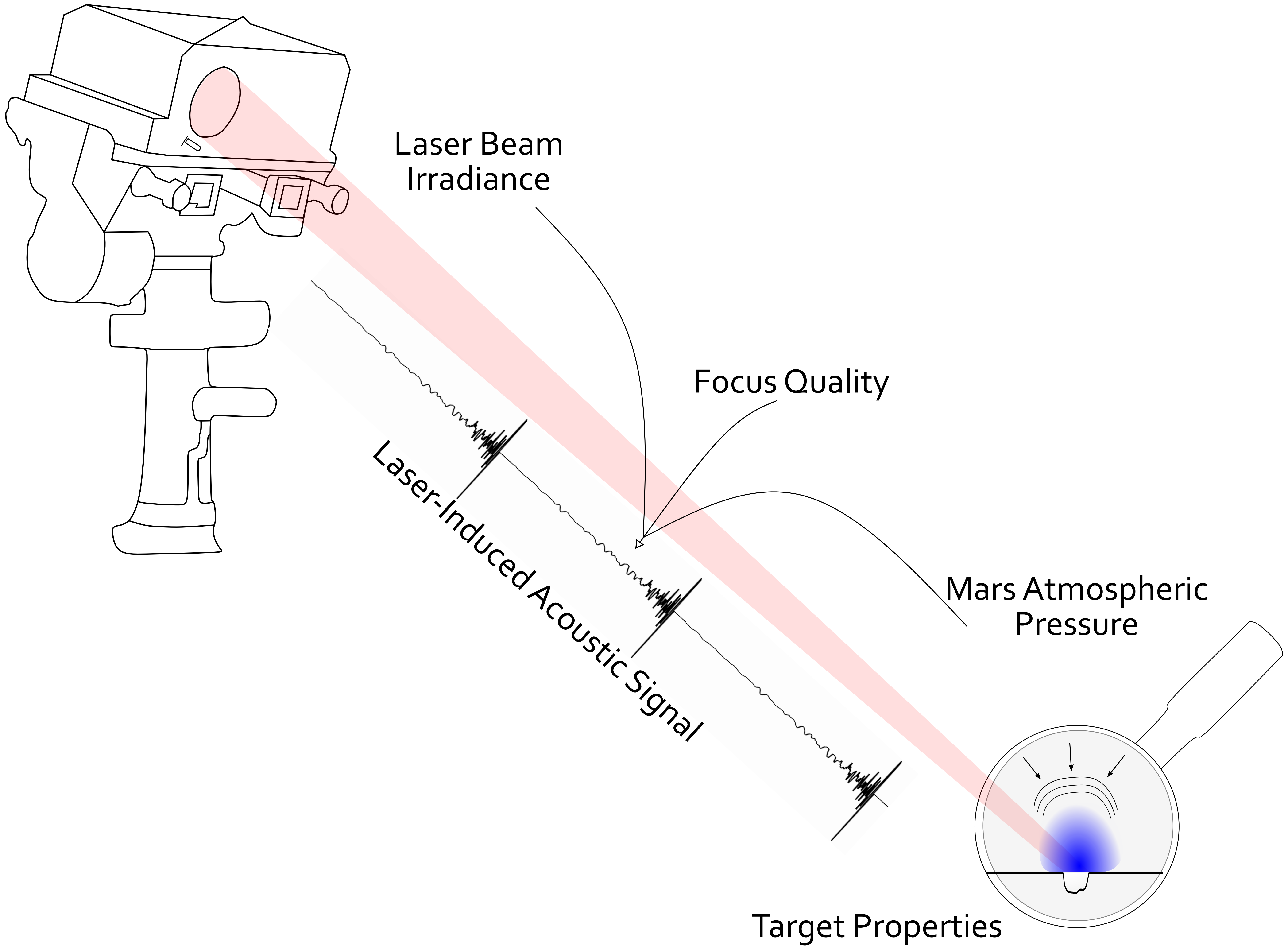

Recording Laser-Induced Sparks on Mars to...

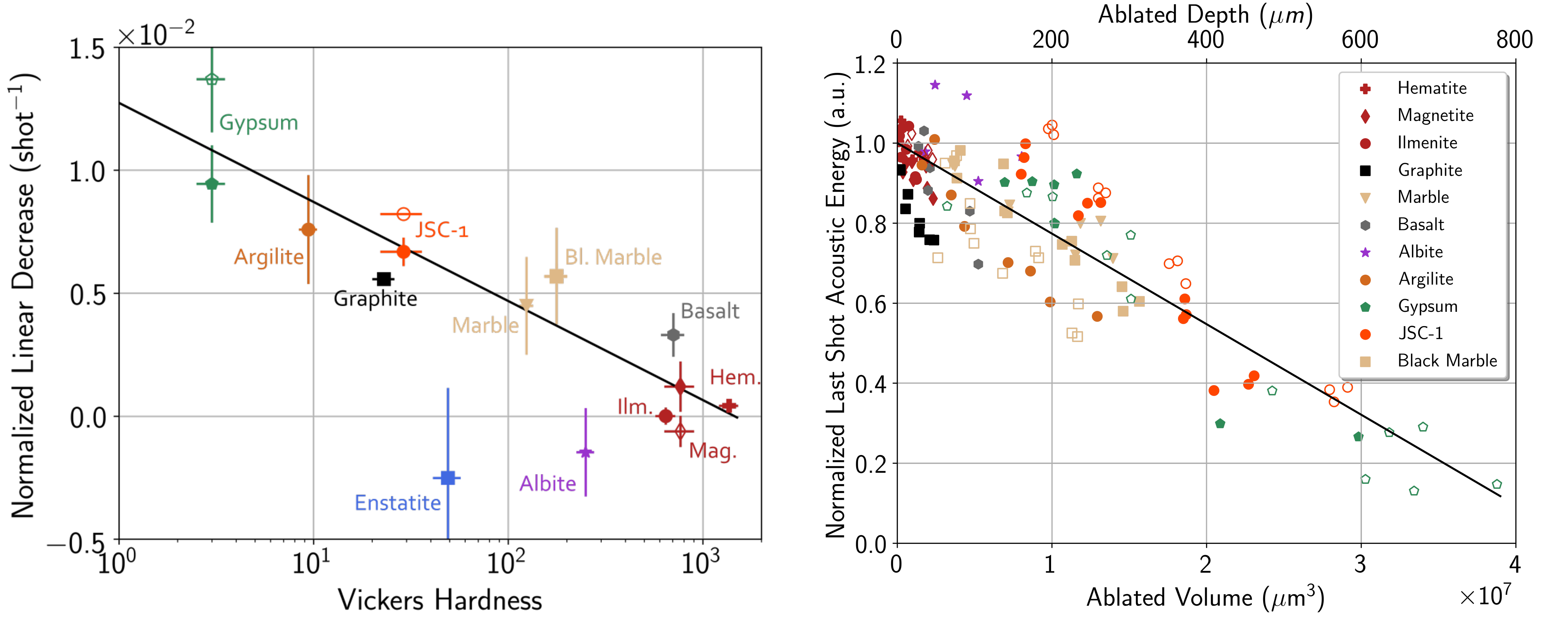
Estimate target hardness

Measure ablated volume